ARTICLE

doi:10.1038/nature16187

Autophagy maintains stemness by preventing senescence

Laura García-Prat[1], Marta Martínez-Vicente[2]*, Eusebio Perdiguero[1], Laura Ortet[1], Javier Rodríguez-Ubreva[3], Elena Rebollo[4], Vanessa Ruiz-Bonilla[1], Susana Gutarra[1], Esteban Ballestar[3], Antonio L. Serrano[1], Marco Sandri[5,6]* & Pura Muñoz-Cánoves[1,7]

During ageing, muscle stem-cell regenerative function declines. At advanced geriatric age, this decline is maximal owing to transition from a normal quiescence into an irreversible senescence state. How satellite cells maintain quiescence and avoid senescence until advanced age remains unknown. Here we report that basal autophagy is essential to maintain the stem-cell quiescent state in mice. Failure of autophagy in physiologically aged satellite cells or genetic impairment of autophagy in young cells causes entry into senescence by loss of proteostasis, increased mitochondrial dysfunction and oxidative stress, resulting in a decline in the function and number of satellite cells. Re-establishment of autophagy reverses senescence and restores regenerative functions in geriatric satellite cells. As autophagy also declines in human geriatric satellite cells, our findings reveal autophagy to be a decisive stem-cell-fate regulator, with implications for fostering muscle regeneration in sarcopenia.

The regenerative capacity of skeletal muscle relies on long-lived Pax7-expressing muscle stem cells (called satellite cells), which are normally in quiescence (a G0 reversible arrest state). In response to tissue damage, these cells activate, enter the cell cycle and either expand and form new myofibres or self-renew to restore the quiescent satellite cell pool[1–4]. Quiescence therefore appears to be a simple way of functionally maintaining the stem-cell population throughout life in the absence of regenerative demand, particularly in tissues with little turnover, such as skeletal muscle.

Sarcopenia, the age-related loss of skeletal muscle mass and function, is maximal at geriatric age. At this last stage of life, skeletal muscle shows a profound regenerative impairment that contributes to the individual's physical incapacitation. Both changes in the environment (such as inflammatory status) and/or satellite-cell-intrinsic mechanisms associated to ageing may contribute to this regenerative decline[5,6]. Recent studies have demonstrated that aged skeletal muscles fail to retain stem-cell quiescence[7–9]. Both the number and the functionality of muscle stem cells decline with ageing[7–13], with satellite cells switching from a quiescence to a pre-senescence state in sarcopenic muscle at geriatric age[8]. How satellite cells maintain quiescence during their long life and avoid acquisition of the senescence program until advanced age is largely unknown.

Using physiologically aged mice, we show that quiescent muscle stem cells preserve their integrity over time through active maintenance of organelle and protein homeostasis (proteostasis) as a cellular quality control mechanism. We demonstrate that these dormant stem cells display continuous basal macroautophagy (hereafter referred to as 'autophagy'; that is, the process for degradation of long-lived proteins and damaged organelles in lysosomes[14,15]). This activity declines during ageing. Physiological decline of autophagy in old satellite cells or its genetic impairment in young cells, results in toxic cellular waste accumulation, resulting in entry into senescence.

Our studies indicate that muscle stem cells preserve their G0-reversible quiescence state from entering a G0-irreversible senescence state through autophagy. Genetic and pharmacological regimes that reinstall basal autophagy in geriatric mice reversed stem-cell senescence and restored regeneration, which has implications for the use of regenerative medicine in sarcopenia.

Impaired autophagy in aged satellite cells

We interrogated the transcriptomes of quiescent satellite cells compared to activated cells for changes in proteostasis genes[16–18] and uncovered autophagy as the most prevalent pathway in the quiescent state (Extended Data Fig. 1a and Supplementary Table 1). *K*-means clustering analysis revealed an age-associated downregulation of autophagic genes in quiescence (Extended Data Fig. 1b and Supplementary Table 1).

Autophagy is an evolutionary conserved process of self-degradation of cellular components (organelles, cytosol portions and misfolded proteins) by autophagosomes, which are delivered to the lysosomal machinery, thus preventing waste accumulation[14,15], and this process has been implicated in ageing of different model organisms[14,15,19,20]. To investigate the occurrence of autophagy in quiescent muscle stem cells we used green fluorescent protein (GFP)–LC3 (a well-known marker of autophagosomes) transgenic mice[21,22]. Quiescent satellite cells were isolated by fluorescence-activated cell sorting (FACS) (Extended Data Fig. 1c) from the resting muscle of young (3 months) and old (20–24 months) GFP–LC3 mice. Punctate GFP–LC3 signal was found in young cells, and this was increased in old cells (Fig. 1a, Extended Data Fig. 1d and Supplementary Videos 1 and 2). We next used the autophagy-flux inhibitor bafilomycin, which prevents lysosome degradation, thus increasing punctate GFP–LC3 exclusively when autophagy is active[23]. Bafilomycin treatment demonstrated that—in contrast to the result for young cells—old satellite cells lacked the capacity for further autophagosome formation, as monitored by GFP–LC3 fluorescence levels (Fig. 1b). These results indicate constitutive autophagic activity in young quiescent satellite cells and impaired autophagic activity during ageing. Fluorescence, transmission-electron microscopy and western

[1]Cell Biology Group, Department of Experimental and Health Sciences, Pompeu Fabra University (UPF), CIBER on Neurodegenerative diseases (CIBERNED), E-08003 Barcelona, Spain. [2]Neurodegenerative Diseases Research Group, Vall d'Hebron Research Institute-CIBERNED, E-08035 Barcelona, Spain. [3]Chromatin and Disease Group, Cancer Epigenetics and Biology Programme (PEBC), Bellvitge Biomedical Research Institute (IDIBELL), L'Hospitalet de Llobregat, E-08907 Barcelona, Spain. [4]Advanced Fluorescence Microscopy Unit, Molecular Biology Institute of Barcelona (IBMB-CSIC), E-08028 Barcelona, Spain. [5]Department of Biomedical Science, University of Padova, 35100 Padova, Italy. [6]Telethon Institute of Genetics and Medicine (TIGEM), 80131 Napoli, Italy. [7]ICREA, E-08908 Barcelona, Spain.
*These authors contributed equally to this work.

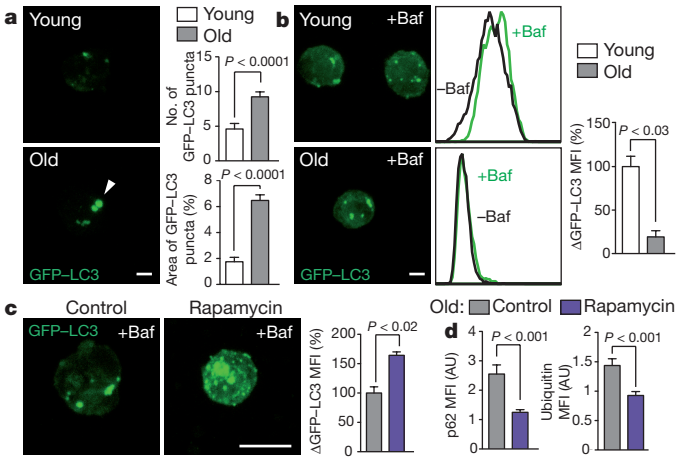

Figure 1 | Altered basal autophagy in ageing muscle stem cells. **a**, Number and area of punctate GFP–LC3 in quiescent satellite cells. Arrowheads, autophagic vesicles. **b**, Autophagy flux in cells from **a**. Cells were treated with vehicle or bafilomycin (+Baf) for 4 h before analysis. The change in mean fluorescence intensity (MFI) of GFP–LC3 in cells treated with bafilomycin is shown. **c**, Autophagy flux in quiescent satellite cells from old GFP–LC3 mice treated for two weeks with rapamycin or vehicle control. Satellite cells ± bafilomycin treatment as in **b**. **d**, p62 and ubiquitin (Ub) MFI from cells of the GFP–LC3 mice treated as in **c**. AU, arbitrary units. Data show mean ± s.e.m. Comparisons by two-sided Mann–Whitney *U*-test. Sample numbers were $n = 51$ (young), $n = 106$ (old) cells analysed from 3 animals for **a**; $n = 60{,}000$ cells from 3 animals for **b**; $n = 60{,}000$ cells from 3 animals for **c**; $n = 36$ (control), 39 (rapamycin treated) cells from 3 animals for **d**. The *z* projections of representative images are shown. Scale bars are all 1.5 μm, apart from 5 μm for **c**.

blotting analyses indicated common traits of deficient autophagy in old satellite cells, including the accumulation of autophagic vesicles (Extended Data Fig. 1e, f), aggregates forming of p62 (a protein regulating autophagic clearance of dysfunctional organelles or aggregates), ubiquitin (Ub)-positive inclusions (Extended Data Fig. 1g), reduced LC3II accumulation after bafilomycin treatment (Extended Data Fig. 1h). A two-week-treatment in old mice with rapamycin (or spermidine), well-known autophagy-inducing regimes[24,25], restored basal autophagy in stem cells (Fig. 1c, Extended Data Fig. 1i and Supplementary Videos 3 and 4) and reduced protein and organelle aggregates (Fig. 1d and Extended Data Fig. 1j).

Restoring autophagy prevents senescence

Satellite cells enter a senescent state when they reach a geriatric age (over 28 months in mice)[8,26]. We investigated whether dysregulated basal autophagy may underlie the loss of bona fide quiescence. Using an mRFP–GFP–LC3 construct[27] (a tandem fluorescent-tagged LC3 reporter containing monomeric red fluorescent protein (mRFP) and GFP), transfected into young, old and geriatric satellite cells, analysing these samples in combination with bafilomycin treatment, we found a higher blockade of autophagic flux in geriatric than old cells, with respect to young cells (the blockade is geriatric > old > young). In the absence of bafilomycin, red LC3 puncta (mature autolysosomes) were only abundant in young cells. Bafilomycin treatment induced yellow LC3 puncta (non-fused autophagosomes) accumulation in young cells, which was blunted in old and geriatric cells (Fig. 2a). Geriatric satellite cells also showed increased co-localization of p62–ubiquitin aggregates in non-degraded autophagosomes (Fig. 2b). As p62 marks damaged organelles for degradation by selective autophagy, whereas ubiquitin marks substrates for their degradation by either the ubiquitin–proteasome system (UPS) or selective autophagy, the increased signal of both proteins and their co-localization demonstrates that the autophagic defect in these cells is due, at least in part, to a block in autophagosomal or lysosomal clearance.

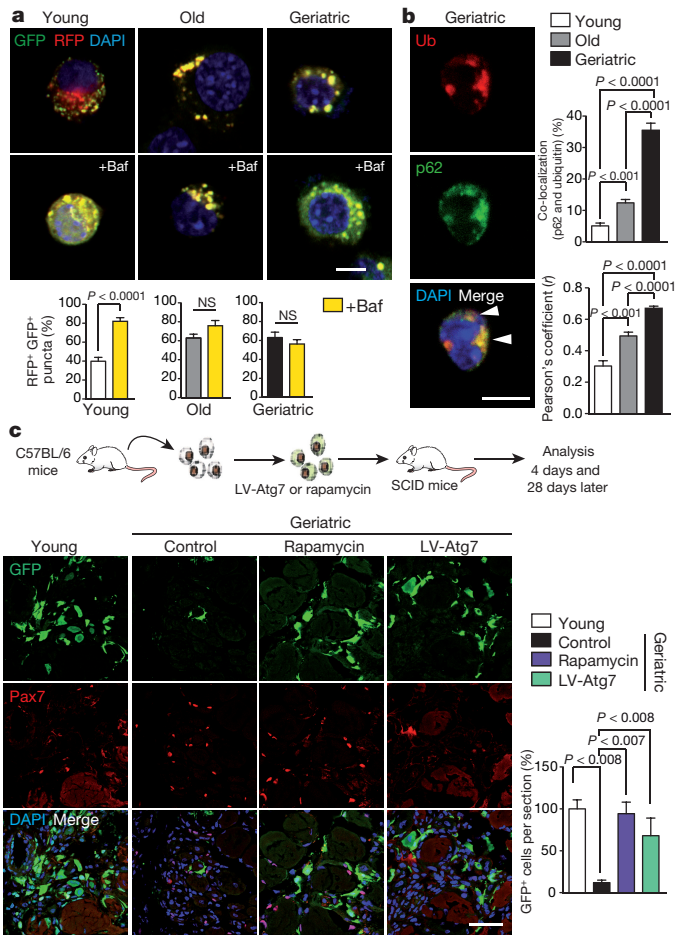

Figure 2 | Defective autophagy causes numerical and functional satellite cell decline in ageing. **a**, The mRFP–GFP–LC3 plasmid was transfected into young (3 months), old (24 months) and geriatric (28 months) satellite cells to enable the detection of autophagosomes (yellow) and their maturation into autolysosomes (red) in the presence or absence of bafilomycin treatment (as in Fig. 1b). The graph indicates the percentage of double-positive puncta (RFP^+/GFP^+) (autophagosomes) out of total puncta (RFP^+/GFP^+, RFP^+, autophagosomes and autolysosomes). **b**, Quantification of p62 and ubiquitin aggregates in quiescent satellite cells from **a**. Co-localization staining area with respect to total cellular area. Pearson's coefficient (*r*) indicates the correlation of intensity values of red and green pixels in dual-channel images. Arrowheads indicate co-localization. **c**, An equal number of LV-GFP-infected satellite cells from young or geriatric mice, treated for 48 h with rapamycin or LV-Atg7 infected (or controls), were transplanted into an injured mouse muscle, and analysed 4 or 28 days later (for analysis on day 28, see Extended Data Fig. 2i, j). Analysis on day 4 of GFP and Pax7 immunostaining. Quantification of GFP^+ cells per muscle field. Values relative to transplanted young cells (100%). Data show mean ± s.e.m. Comparisons by two-sided Mann–Whitney *U*-test. The sample numbers were $n = 21$ (young), $n = 19$ (young, +bafilomycin), $n = 30$ (old), $n = 15$ (old, +bafilomycin), $n = 21$ (geriatric) and $n = 15$ (geriatric, +bafilomycin) cells analysed from 3 animals for **a**; $n = 35$ (young), $n = 66$ (old) and $n = 104$ (geriatric) cells from 3 animals for **b**; $n = 5$ engraftments per group for **c**. Representative images are shown. The *z* projections of representative images are shown. Scale bars are all 5 μm, apart from 50 μm for **c**.

To investigate whether restoring autophagy could rescue the cell-intrinsic irreversible cell cycle and regenerative block of geriatric cells, we engrafted freshly isolated GFP-labelled young and geriatric satellite cells (pre-treated with rapamycin or the control vehicle) into pre-injured muscles of young recipient mice. Autophagy reactivation significantly restored expansion of geriatric cells (expressing Pax7, Ki67, MyoD or myogenin (Mgn, also known as Myog)) after a four-day engraftment (Fig. 2c and Extended Data Fig. 2a–c) and prevented senescence

(geroconversion), as shown by $p16^{INK4a}$ and γH2AX reduction (Extended Data Fig. 2d). Rapamycin (or spermidine) treatment also decreased geriatric senescent cells (senescence-associated β-galactosidase-positive (SA-β-gal$^+$)) (Extended Data Fig. 2e, f) and re-established proliferation (Extended Data Fig. 2e). A genetic approach to enhance autophagy, by overexpressing Atg7 (crucial for autophagosome formation) (Fig. 2c and Extended Data Fig. 2g, h) rescued the proliferative defect, while reducing senescence (Extended Data Fig. 2e). Furthermore, satellite cell transplantation and whole-muscle graft experiments demonstrated that the introduction of Atg7 alone in geriatric satellite cells rescued their intrinsic regenerative capacity, allowing the formation of new muscle fibres (Fig. 2c and Extended Data Fig. 2i, j).

Atg7 loss causes stem-cell senescence

To investigate if basal autophagy disruption causally breaks quiescence, we intercrossed Atg7-floxed mice with Pax7-Cre and Pax7-Cre^{ER} mice, to impair autophagy in Pax7-expressing cells either constitutively ($Atg7^{\Delta Pax7}$) or inducibly ($Atg7^{\Delta Pax7ER}$) after tamoxifen administration. Intercrossing $Atg7^{\Delta Pax7}$ with GFP–LC3 mice ($Atg7^{\Delta Pax7}$:GFP–LC3) resulted in the loss of autophagosomes in quiescent *Atg7* null satellite cells (Extended Data Fig. 3a, b). The satellite cell pool was severely reduced in $Atg7^{\Delta Pax7}$ mice (Fig. 3a and Extended Data Fig. 3c). Tamoxifen administration to three-month-old $Atg7^{\Delta Pax7ER}$ mice led to satellite cell loss after 30 days (Fig. 3b), indicating that basal autophagy is required for both establishment and maintenance of the adult quiescent stem-cell population. The remaining $Atg7^{\Delta Pax7ER}$ satellite cells showed unexpected signs of premature ageing including induction of $p16^{INK4a}$, $p21^{CIP1}$ and $p15^{INK4b}$ and DNA damage (γH2AX$^+$ cells) (Fig. 3c, d and Extended Data Fig. 3d). $Atg7^{\Delta Pax7}$ satellite cells did not undergo mitotic or myogenic differentiation pathways (Extended Data Fig. 3e). Thus, loss of autophagy with ageing may be the cause underlying the age-associated numerical decline in muscle stem cells[7,8,10–13].

In response to muscle injury, Pax7$^+$ cells from young $Atg7^{\Delta Pax7}$ mice showed reduced activation and expansion capacity (Fig. 3e and Extended Data Fig. 3f), and accelerated entry into deep senescence[26,28] (geroconversion[29]) *in vivo* and *in vitro*, as demonstrated by SA-β-gal-staining (Fig. 3f), and increased expression of γH2AX and phosphorylated S6, and also evidence of regenerative failure, shown by reduced cell proliferation and decreased size of regenerating fibres (Fig. 3g and Extended Data Fig. 3g–l). Confirming the cell-intrinsic regenerative failure, fewer GFP$^+$ fibres derived from *Atg7* null satellite cells were found in transplantation experiments (Extended Data Fig. 3m, n), and this failure could not be rescued by rapamycin (or spermidine) (Extended Data Fig. 3m–o).

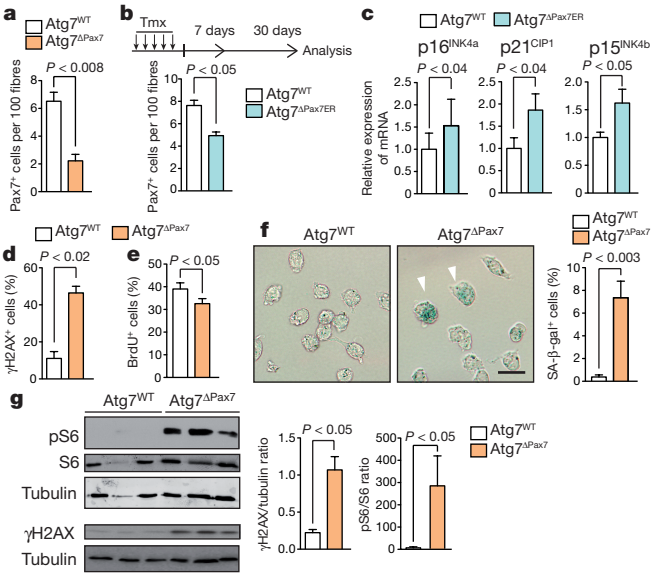

Figure 3 | Genetic impairment of autophagy disrupts satellite cell homeostasis. a, Satellite cell quantification by analysis of Pax7 immunostaining of muscles in three-month-old $Atg7^{WT}$ and $Atg7^{\Delta Pax7}$ mice. **b**, Schematic of the mouse tamoxifen (Tmx) treatment and satellite cell analysis. Satellite cell quantification in $Atg7^{WT}$/$Atg7^{\Delta Pax7ER}$ mice on day 30 after tamoxifen treatment as in **a**. **c**, RT–qPCR of senescence markers (7 days after tamoxifen treatment) in cells from **b**. **d**, The percentage of co-localizing γH2AX$^+$ cells out of the total Pax7$^+$ cells in **a**. **e**, **f**, Quantification of BrdU$^+$ (**e**) and SA-β-gal$^+$ (**f**) cells isolated from mice in **a**. The arrowhead indicates positive staining. **g**, Western blotting of cells from **a**; for a full scan of the gel see Supplementary Fig. 1. pS6, phosphorylated S6. Data show mean ± s.e.m. Comparisons by two-sided Mann–Whitney *U*-test. Sample numbers were: $n = 5$ animals per group for **a**; $n = 3$ animals per group for **b**–**g**. Representative images are shown. The *z* projections of representative images are shown. Scale bars, 250 μm.

Altered mitophagy and increased ROS induce senescence

We next investigated how loss of autophagy in young quiescent satellite cells induced premature ageing. Genetic disruption of autophagy in satellite cells resulted in a similar phenotype to that observed in aged cells with rapid accumulation of p62 and ubiquitin-positive aggregates, and also mitochondria and lysosomes (MitoTracker, and LysoTracker and Lamp1) (Fig. 4a, b and Extended Data Fig. 4a). There was also a lower proportion of healthy mitochondria in old (and $Atg7^{\Delta Pax7ER}$) satellite cells, as revealed by reduced membrane potential (a lower mean fluorescence intensity ratio of the active mitochondria labelling fluorescent dye TMRM to MitoTracker green) (Fig. 4a, b). Furthermore, mitophagy (the cellular capacity to clear damaged mitochondria by autophagy) was defective in geriatric satellite cells, as indicated by mitochondria accumulation inside autophagosomes or lysosomes (through co-localization of mitochondrial TOM20 and lysosomal Lamp-1 markers) (Extended Data Fig. 4b). *In vivo* rapamycin (or spermidine) treatment of geriatric mice restored mitophagy in satellite cells (Extended Data Fig. 4b–f). Consistent with age-impaired mitophagy, young, but not geriatric, cells were capable of eliminating carbonyl

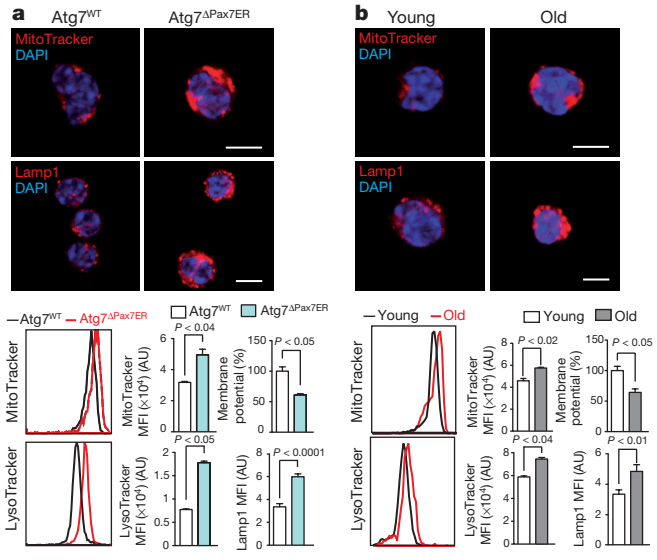

Figure 4 | Autophagy loss results in mitochondrial dysfunction and accumulation of organelles, proteins and ROS. a, Lysosomal (Lamp1 and LysoTracker) and mitochondrial (MitoTracker) quantification in satellite cells from $Atg7^{WT}$ and $Atg7^{\Delta Pax7ER}$ mice, one month after tamoxifen treatment. Membrane potential monitored as the mean fluorescent intensity ratio of TMRM to MitoTracker Green. **b**, Similar quantification as in **a** for young and old satellite cells. Membrane potential analysis as in **a**. Data show mean ± s.e.m. Comparisons by two-sided Mann–Whitney *U*-test. The sample numbers were $n = 60{,}000$ cells analysed from 3 animals for **a** and **b**. Representative images are shown. The *z* projections of representative images are shown. Scale bars, 5 μm.

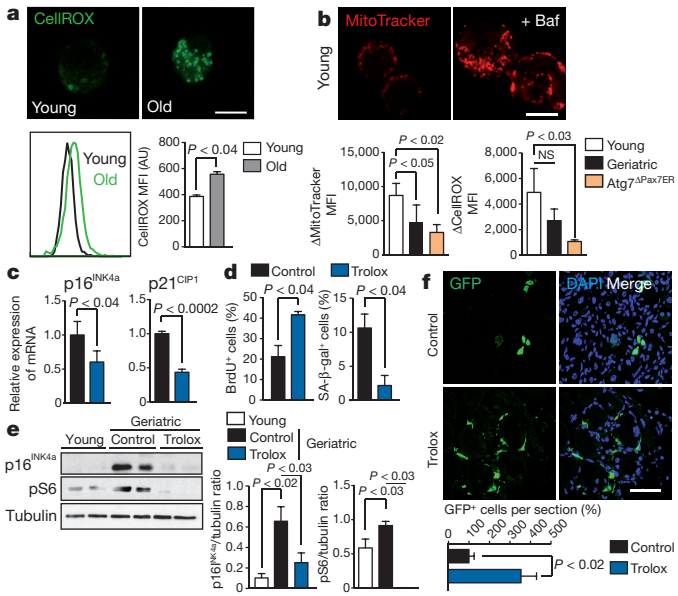

Figure 5 | ROS inhibition prevents senescence in aged satellite cells. **a**, ROS quantification in young and old satellite cells by CellROX flow cytometry. **b**, Mitochondria (MitoTracker) and ROS (CellROX) in satellite cells, ± 24 h bafilomycin treatment. Results represent increased MFI in the presence of bafilomycin. Representative images of young satellite cells. **c**, RT–qPCR of senescence markers ± Trolox. **d**, Quantification of $BrdU^+$ and SA-β-gal^+ cells from **c**, pretreated with Trolox (or controls that were not treated with Trolox), and cultured for 96 h. **e**, Western blotting in cells ± Trolox; for full-scan of gel see Supplementary Fig. 1. **f**, Geriatric cells ± Trolox 48 h pre-treatment, were transplanted and analysed as in Fig. 2c. Data show mean ± s.e.m. Comparisons by two-sided Mann–Whitney *U*-tests. Sample numbers were $n = 60{,}000$ cells analysed from 3 animals for **a** and **b**; $n = 3$ animals per group for **c**–**e**; $n = 4$ engraftments per group for **f**. Representative images are shown. The *z* projections of representative images are shown. Scale bars are all 5 μm apart from 50 μm for **f**.

cyanide 3-chlorophenylhydrazone (CCCP)-damaged mitochondria (Extended Data Fig. 4d, e).

Next, we analyzed how altered mitophagy led to satellite cell senescence with ageing. We detected higher levels of reactive-oxygen species (ROS), parkin (marking damaged mitochondria for degradation by mitophagy), and DNA-damage markers in Atg7-deficient satellite cells (Fig. 3d, g and Extended Data Figs 3h and 5a, b), associated with $p16^{INK4a}$ and pS6 induction (Fig. 3g and Extended Data Figs 3g and 4h). Higher ROS labelling and ROS–mitochondria co-localization were also observed in geriatric satellite cells, correlating with impaired mitophagic flux (Fig. 5a and Extended Data Fig. 4g). Bafilomycin-induced autophagy block caused greater mitochondrial accumulation in young cells, compared with geriatric and $Atg7^{\Delta Pax7ER}$ cells, paralleling the ROS increase (Fig. 5b). To address the role of ROS in impaired autophagy, we inhibited it with Trolox (a vitamin E analogue) (Extended Data Fig. 5c). Trolox treatment of old GFP–LC3 mice increased GFP–LC3 puncta (after bafilomycin treatment) and reduced p62 and ubiquitin aggregates and mitochondria–ROS co-localization in GFP–LC3 satellite cells (Extended Data Figs 4g and 5d). Attenuation of autophagic block by ROS inhibition was further confirmed in bafilomycin-treated aged cells through LC3-II accumulation (Extended Data Fig. 5e, f) and an mRFP–GFP–LC3 tandem reporter, which detected reduced autophagosomes (RFP^+/GFP^+ puncta) and rescued autophagic flux (Extended Data Fig. 5g). Trolox treatment prevented the appearance of senescence markers (Fig. 5c–e), restored the expansion (Fig. 5d), and rescued the cell-intrinsic proliferative and regenerative defect of geriatric satellite cells after transplantation (Fig. 5f and Extended Data Fig. 5h). Thus, increased ROS, resulting from impaired autophagy, drive satellite cell senescence in aged cells.

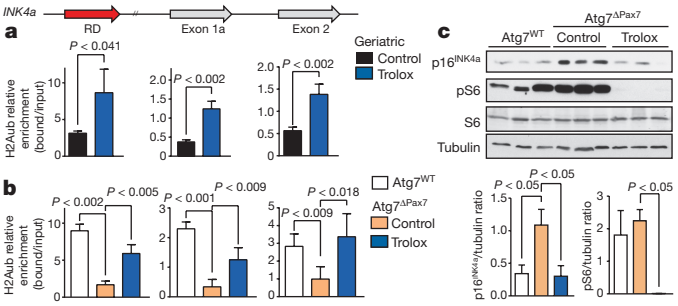

Figure 6 | Epigenetic control of $p16^{INK4a}$ expression by ROS in autophagy-impaired satellite cells. **a**, Chromatin immunoprecipitation (ChIP) for K119 ubiquitination of H2A (H2Aub) in geriatric satellite cells, in the presence or absence of 48 h of Trolox treatment. RD, regulatory domain. **b**, H2Aub-ChIP for $Atg7^{WT}$ and $Atg7^{\Delta Pax7}$ satellite cells treated as in **a**. **c**, Western blotting for cells in **b**; for full gel scan see Supplementary Fig. 1. Data show mean ± s.e.m. Comparisons by two-sided Mann–Whitney *U*-test. *P* values indicated. Sample numbers were $n = 3$ animals per group for **a**–**c**.

Loss of the polycomb repressive complex-1 (PRC1)-mediated H2A monoubiquitination of lysine 119 (H2Aub) at *INK4a* (also known as *Cdkn2a*) locus drives $p16^{INK4a}$ induction in geriatric satellite cells[8] (Extended Data Fig. 5i). We found that Trolox treatment restored *INK4a* locus H2Aub modification in geriatric and Atg7-deficient satellite cells (Fig. 6a, b), resulting in $p16^{INK4a}$ repression, and this reduced senescence while promoting proliferation (Figs 5c–f and 6c and Extended Data Fig. 5j). Genetic silencing (with short-hairpin RNA) of *INK4a* restored proliferation in $Atg7^{\Delta Pax7}$ satellite cells while reducing the expression of senescence-associated genes and the number of SA-β-gal^+ cells, and augmenting their regenerative capacity (Extended Data Figs 5k and 6a, b). Thus, the ROS-induced $p16^{INK4a}$ axis links impaired autophagy and senescence in ageing satellite cells.

Defective autophagy in aged human cells

Skeletal muscles from geriatric individuals show sarcopenia and presence of senescent satellite cells (Extended Data Fig. 7a, b)[8]. As in mice, human satellite cells from geriatric individuals showed defective protein and organelle clearance, as indicated by p62 and mitochondrial accumulation (Extended Data Fig. 7c, d) compared to young cells, which was tightly associated with increased ROS levels (Extended Data Fig. 7d, e) and SA-β-gal^+ cells (Extended Data Fig. 7f), consistent with reduced proliferative potential (Extended Data Fig. 7g). The causal role of impaired autophagy on the geroconversion of ageing human satellite cells under proliferative pressure was supported by the capacity of rapamycin to revert the abnormal mitochondrial content, protein aggregates and ROS (Extended Data Fig. 7c, d), and senescence phenotype (Extended Data Fig. 7f–i). Thus, restoration of autophagy and organelle homeostasis in aged human satellite cells suffices to rescue senescence, as is the case in murine satellite cells.

Discussion

In tissues with little turnover, reversible quiescence is the normal stem-cell state throughout life. However, quiescence is known to be progressively lost with ageing due to systemic/niche- and intrinsic-factor alterations[2,7]. Recent studies showed that at geriatric age, the normal stem-cell quiescent state is substituted by an irreversible senescence state, which results in a numerical and functional decline of stem cells[8]. The mechanisms accounting for the maintenance of quiescence, preservation of the stem-cell pool and prevention of senescence during an individual's life remain unknown. Our results demonstrate that quiescent satellite cells are equipped with cytoprotective and cellular quality-control mechanisms that actively repress the senescence program, thereby preserving the integrity and fitness of cells. We provide evidence of loss of autophagy in satellite cells that occurs with ageing,

resulting in accumulation of damaged proteins and organelles, leading to senescence and stem-cell exhaustion. Consistent with this finding, genetic inhibition of autophagy specifically in satellite cells of young mice caused rapid entry into senescence, resulting in numerical and functional exhaustion of stem cells, and defective muscle regeneration. These findings were surprising, considering that a decline in basal autophagy in quiescent stem cells of physiologically aged mammalian organisms has not been described before. Autophagy is usually considered to be an effector pathway, rather than a cause, of senescence, particularly in oncogene-induced senescence[30–33].

How autophagy balances quiescence and senescence in muscle stem cells is unknown. Here we show that in adult resting muscle, quiescent stem cells attenuate proteotoxicity by maintaining a high basal autophagy flux, constituting a homeostatic 'clean up' process. This function is particularly critical in non-dividing stem cells, in which mitotic dilution of intracellular toxic debris does not take place[20,34]. Autophagy failure in aged resting stem cells leads to accumulation of damaged proteins and dysfunctional organelles, specially mitochondria, which generates enhanced ROS levels that cause DNA damage and senescence entry, consistent with previous studies[35–42]. Indeed, we uncover ROS as a key epigenetic regulator of the senescence-promoting gene *INK4a* in ageing stem cells, by impeding PRC1-mediated lysine 119 H2A ubiquitination, the required epigenetic mark for *INK4a* locus silencing. Consistent with this, treatment of geriatric mice (and mice with satellite-cell-specific *Atg7* deficiency) with antioxidants not only restored PRC1-mediated *INK4a* locus repression and prevented satellite cell senescence, but also restored regenerative capacity. Signs of impaired autophagy and loss of proteostasis, correlating with senescence and defective myogenic functions, were also observed in human satellite cells from geriatric individuals.

At variance with our findings, a recent study demonstrated that, upon *in vitro* stress, autophagy does not decline, but is even induced in haematopoietic stem cells with ageing, consistent with maintenance of haematopoietic stem cell number[43]. Thus, we propose that long-lived quiescent stem cells within low turnover tissues primarily rely on autophagy to preserve fitness and avoid senescence, and that stem cells of skeletal muscle in particular lose this protection during ageing (Extended Data Fig. 7j). Notably, a recent study also reported that autophagy is needed for the activation of young satellite cells[44]. Furthermore, in the whole musculature, age-associated myofibre degeneration and mitochondrial dysfunction could also be alleviated by autophagy reactivation[19,45].

Our studies thus demonstrate that autophagy is a decisive factor in the switch between the quiescence and senescence fate of muscle stem cells (Extended Data Fig. 7j). Although ageing-induced senescence is often viewed as an inescapable and irremediable process, we provide evidence that *in vivo* restoration of constitutive autophagy (or neutralization of excessive ROS) averts intracellular damage accumulation, and prevents satellite cell senescence and functional decline in old mice, as well as in aged human stem cells, reinforcing the notion that the intrinsic-ageing clock in stem cells can be pharmacologically manipulated.

Online Content Methods, along with any additional Extended Data display items and Source Data, are available in the online version of the paper; references unique to these sections appear only in the online paper.

Received 21 November 2014; accepted 29 October 2015.

1. Cheung, T. H. & Rando, T. A. Molecular regulation of stem cell quiescence. *Nature Rev. Mol. Cell Biol.* **14,** 329–340 (2013).
2. Comai, G. & Tajbakhsh, S. Molecular and cellular regulation of skeletal myogenesis. *Curr. Top. Dev. Biol.* **110,** 1–73 (2014).
3. Yin, H., Price, F. & Rudnicki, M. A. Satellite cells and the muscle stem cell niche. *Physiol. Rev.* **93,** 23–67 (2013).
4. Montarras, D., L'Honore, A. & Buckingham, M. Lying low but ready for action: the quiescent muscle satellite cell. *FEBS J.* **280,** 4036–4050 (2013).
5. Grounds, M. D. Therapies for sarcopenia and regeneration of old skeletal muscles: more a case of old tissue architecture than old stem cells. *Bioarchitecture.* **4,** 81–87 (2014).
6. García-Prat, L., Sousa-Victor, P. & Muñoz-Cánoves, P. Functional dysregulation of stem cells during aging: a focus on skeletal muscle stem cells. *FEBS J.* **280,** 4051–4062 (2013).
7. Chakkalakal, J. V., Jones, K. M., Basson, M. A. & Brack, A. S. The aged niche disrupts muscle stem cell quiescence. *Nature* **490,** 355–360 (2012).
8. Sousa-Victor, P. *et al.* Geriatric muscle stem cells switch reversible quiescence into senescence. *Nature* **506,** 316–321 (2014).
9. Sousa-Victor, P., Garcia-Prat, L., Serrano, A. L., Perdiguero, E. & Muñoz-Cánoves, P. Muscle stem cell aging: regulation and rejuvenation. *Trends Endocrinol. Metab.* **26,** 287–296 (2015).
10. Cosgrove, B. D. *et al.* Rejuvenation of the muscle stem cell population restores strength to injured aged muscles. *Nature Med.* **20,** 255–264 (2014).
11. Bernet, J. D. *et al.* p38 MAPK signaling underlies a cell-autonomous loss of stem cell self-renewal in skeletal muscle of aged mice. *Nature Med.* **20,** 265–271 (2014).
12. Price, F. D. *et al.* Inhibition of JAK–STAT signaling stimulates adult satellite cell function. *Nature Med.* **20,** 1174–1181 (2014).
13. Tierney, M. T. *et al.* STAT3 signaling controls satellite cell expansion and skeletal muscle repair. *Nature Med.* **20,** 1182–1186 (2014).
14. Cuervo, A. M. *et al.* Autophagy and aging: the importance of maintaining "clean" cells. *Autophagy* **1,** 131–140 (2005).
15. He, C. & Klionsky, D. J. Regulation mechanisms and signaling pathways of autophagy. *Annu. Rev. Genet.* **43,** 67–93 (2009).
16. Fukada, S. *et al.* Molecular signature of quiescent satellite cells in adult skeletal muscle. *Stem Cells* **25,** 2448–2459 (2007).
17. Liu, L. *et al.* Chromatin modifications as determinants of muscle stem cell quiescence and chronological aging. *Cell Rep.* **4,** 189–204 (2013).
18. Pallafacchina, G. *et al.* An adult tissue-specific stem cell in its niche: a gene profiling analysis of *in vivo* quiescent and activated muscle satellite cells. *Stem Cell Res.* **4,** 77–91 (2010).
19. Carnio, S. *et al.* Autophagy impairment in muscle induces neuromuscular junction degeneration and precocious aging. *Cell Rep.* **8,** 1509–1521 (2014).
20. Rubinsztein, D. C., Marino, G. & Kroemer, G. *Autophagy and aging. Cell* **146,** 682–695 (2011).
21. Mizushima, N., Yamamoto, A., Matsui, M., Yoshimori, T. & Ohsumi, Y. *In vivo* analysis of autophagy in response to nutrient starvation using transgenic mice expressing a fluorescent autophagosome marker. *Mol. Biol. Cell* **15,** 1101–1111 (2004).
22. Klionsky, D. J. *et al.* Guidelines for the use and interpretation of assays for monitoring autophagy in higher eukaryotes. *Autophagy* **4,** 151–175 (2008).
23. Zhu, J., Dagda, R. K. & Chu, C. T. Monitoring mitophagy in neuronal cell cultures. *Methods Mol. Biol.* **793,** 325–339 (2011).
24. Mammucari, C. *et al.* FoxO3 controls autophagy in skeletal muscle *in vivo*. *Cell Metab.* **6,** 458–471 (2007).
25. Morselli, E. *et al.* Spermidine and resveratrol induce autophagy by distinct pathways converging on the acetylproteome. *J. Cell Biol.* **192,** 615–629 (2011).
26. van Deursen, J. M. The role of senescent cells in ageing. *Nature* **509,** 439–446 (2014).
27. Kimura, S., Noda, T. & Yoshimori, T. Dissection of the autophagosome maturation process by a novel reporter protein, tandem fluorescent-tagged LC3. *Autophagy* **3,** 452–460 (2007).
28. Muñoz-Espín, D. & Serrano, M. Cellular senescence: from physiology to pathology. *Nature Rev. Mol. Cell Biol.* **15,** 482–496 (2014).
29. Blagosklonny, M. V. Selective anti-cancer agents as anti-aging drugs. *Cancer Biol. Ther.* **14,** 1092–1097 (2013).
30. Young, A. R. *et al.* Autophagy mediates the mitotic senescence transition. *Genes Dev.* **23,** 798–803 (2009).
31. Narita, M. *et al.* Spatial coupling of mTOR and autophagy augments secretory phenotypes. *Science* **332,** 966–970 (2011).
32. Pérez-Mancera, P. A., Young, A. R. & Narita, M. Inside and out: the activities of senescence in cancer. *Nature Rev. Cancer* **14,** 547–558 (2014).
33. Capparelli, C. *et al.* Autophagy and senescence in cancer-associated fibroblasts metabolically supports tumor growth and metastasis via glycolysis and ketone production. *Cell Cycle* **11,** 2285–2302 (2012).
34. Flach, J. *et al.* Replication stress is a potent driver of functional decline in ageing haematopoietic stem cells. *Nature* **512,** 198–202 (2014).
35. Kodama, R. *et al.* ROS-generating oxidases Nox1 and Nox4 contribute to oncogenic Ras-induced premature senescence. *Genes Cells* **18,** 32–41 (2013).
36. Ramsey, M. R. & Sharpless, N. E. ROS as a tumour suppressor? *Nature Cell Biol.* **8,** 1213–1215 (2006).
37. Ito, K. *et al.* Reactive oxygen species act through p38 MAPK to limit the lifespan of hematopoietic stem cells. *Nature Med.* **12,** 446–451 (2006).
38. Lee, A. C. *et al.* Ras proteins induce senescence by altering the intracellular levels of reactive oxygen species. *J. Biol. Chem.* **274,** 7936–7940 (1999).
39. Mandal, P. K., Blanpain, C. & Rossi, D. J. DNA damage response in adult stem cells: pathways and consequences. *Nature Rev. Mol. Cell Biol.* **12,** 198–202 (2011).
40. Shao, L. *et al.* Reactive oxygen species and hematopoietic stem cell senescence. *Int. J. Hematol.* **94,** 24–32 (2011).
41. Lerner, C. *et al.* Reduced mammalian target of rapamycin activity facilitates mitochondrial retrograde signaling and increases life span in normal human fibroblasts. *Aging Cell* **12,** 966–977 (2013).
42. López-Otín, C., Blasco, M. A., Partridge, L., Serrano, M. & Kroemer, G. The hallmarks of aging. *Cell* **153,** 1194–1217 (2013).
43. Warr, M. R. *et al.* FOXO3A directs a protective autophagy program in haematopoietic stem cells. *Nature* **494,** 323–327 (2013).

44. Tang, A. H. & Rando, T. A. Induction of autophagy supports the bioenergetic demands of quiescent muscle stem cell activation. *EMBO J.* **33,** 2782–2797 (2014).
45. Lee, J. H. *et al*. Sestrin as a feedback inhibitor of TOR that prevents age-related pathologies. *Science* **327,** 1223–1228 (2010).

Supplementary Information is available in the online version of the paper.

Acknowledgements We are indebted to G. Mariño for the gift of GFP–LC3 transgenic mice, C. Keller and M. Capecchi for Pax–Cre mouse lines, J. Ruberte for TEM studies help, E. Masliah and K. Kosberg for Atg7 lentivirus; M. Raya, M. Jardí, and V. Lukesova for their technical contributions, and especially J. Guerra for help in microarray experiments and P. Sousa-Victor for initial findings; J. Martín-Caballero (PRBB Animal Facility) and O. Fornas (UPF/CRG FACS Facility) for technical help, and the KS Society. The authors acknowledge funding from MINECO, Spain (SAF2012-38547, SAF2015-67369-R, PLE2009-0124; SAF2009-08374; "María de Maeztu" Programme for Units of Excellence in R&D MDM-2014-0370), AFM, E-Rare/ERANET, Fundació Marató TV3, MDA, EU-FP7 (Myoage, Optistem and Endostem) and DuchennePP-NL. M.M.-V. acknowledges funding from ISCIII, Spain (FIS-PS09/01267, FIS-PI13/02512, CP09/00184, PI14/01529) and CIBERNED; and MS from the European Union ERC (282310-MyoPHAGY) and Foundation Leducq. L.G.-P. was supported by a Predoctoral Fellowship from Programa de Formación de Personal Investigador (Spain).

Author Contributions L.G.-P. designed and performed most experiments, analysed data, interpreted results and wrote the manuscript. A.L.S. and E.P. designed and performed experiments, and helped in interpreting results and editing the manuscript. M.M.-V. and M.S. helped in designing and interpreting some experiments and results and editing the manuscript. L.O., V.R.-B. and S.G. performed some experiments and provided technical support. E.R. provided technical support in microscopy. J.R.-U. and E.B. performed ChIP experiments and helped in interpreting results. P.M.-C. conceived the project, designed experiments, interpreted results and wrote the manuscript.

Author Information Microarray data have been deposited into the NCBI Gene Expression Omnibus under accession number GSE70376. Reprints and permissions information is available at www.nature.com/reprints. The authors declare no competing financial interests. Readers are welcome to comment on the online version of the paper. Correspondence and requests for materials should be addressed to P.M.-C. (pura.munoz@upf.edu).

METHODS

Data reporting. No statistical methods were used to predetermine sample size. The investigators were not blinded to allocation during experiments and outcome assessment.

Mice. Male mice (C57BL/6 (wild-type, WT), LC3–GFP, the offspring of intercrossing *Atg7*$^{f/f}$ with *Pax7*^{Cre} and *Pax7*^{CreER} lines) were used at different ages. GFP–LC3 mice were provided by G. Mariño. Mice with the *Atg7* gene deletion in satellite cells, as an inducible or constitutive deletion , were generated by breeding *Atg7*$^{fl/fl}$ mice (previously described in ref. 46) with the *Pax7*^{Cre} and *Pax7*^{CreER} lines (provided by C. Keller and M. Capecchi, respectively). All animal experiments were approved by the ethics committee of the (Barcelona Biomedical Research Park (PRBB) and by the Catalan Government and used sex-, age- and weight-matched littermate animals.

When needed, Cre activity was induced by intraperitoneal injection (one injection per day for 4 days) with 5 mg per 25 g body weight of tamoxifen (Sigma; 10 mg ml^{-1} in corn oil).

Induction of muscle regeneration. Mice were anaesthetized with ketamine and xylazine (80:10 mg kg^{-1}, intraperitoneally). Regeneration of skeletal muscle was induced by intramuscular injection of cardiotoxin (CTX, Latoxan; 10^{-5} M) in the tibialis anterior muscle of the mice as described[47]. At the indicated times after injury, mice were euthanized and muscles were dissected, frozen in isopentane cooled with liquid nitrogen, and stored at −80 °C until analysis. For GFP immunostaining of samples, muscles were prefixed for 2 h in 2% paraformaldehyde at 4 °C, and were embedded in 15% sucrose overnight at 4 °C and then frozen in isopentane cooled with liquid nitrogen.

Satellite cell isolation by FACS. Muscles were mechanically disaggregated and incubated in Ham's F10 media containing 0.8% collagenase D (Roche) and 0.125% trypsin and EDTA at 37 °C with agitation, for 25 min and the supernatant was then filtered. The digestion procedure was repeated four times and the supernatants were collected. Cells were incubated in lysis buffer (BD Pharm Lyse) for 10 min on ice, re-suspended in PBS with 2.5% goat serum and counted. PE-Cy7-conjugated anti-CD31 (Biolegend 102418), anti-CD11b (Biolegend 101215/16) and anti-Sca-1 (Biolegend 108113/14) antibodies were used to exclude the Lin (−) negative population and Alexa647-conjugated anti-CD34 (BD Pharmigen 560230) and PE-conjugated anti-α7-integrin (Ablab AB10STMW215) were used for double-positive staining of quiescent satellite cells. Cells were sorted using a FACS Aria II (BD). Isolated satellite cells were used either for RNA extraction or were cultured in Ham's F10 supplemented with 30% FBS and bFGF (0.025 μg ml^{-1}) (growth medium) for proliferation assays or plated on glass slides (Thermo Scientific 177402) for immunostaining analysis.

Flow cytometry analysis. FACS isolated satellite cells (see above) were stained with different dyes for flow cytometry analysis. Staining for mitochondria, lysosomes and ROS was performed by incubating cells at 37 °C with 1 μM tetramethylrhodamine, methyl ester TMRM (T-668), 100 nM MitoTracker Green FM (M7514), 100 nM MitoTracker Red CMXRos (M7512), 500 nM LysoTracker Green DND-26 (L7526) and 5 μM CellROX Green reagent (C10444), following the manufacturer's protocols (Invitrogen) and directly analysed without fixing. Cell analysis was performed in FACS LSR Fortesa (Becton Dickinson). For MFI determination, we used the flow cytometry analysis software Flowlogic. MFI refers to the fluorescence intensity of each event (on average) of the selected cell population, in the chosen fluorescence channel.

Whole-transcriptome analysis of FACS-sorted satellite cells. FACS-sorted satellite cells were collected in lysis buffer and RNA extraction was performed using RNeasy Micro kit (Qiagen). The cDNA was used for transcriptome analysis by Agilent SurePrint G3 Mouse GE 8 × 60 K high density microarray slides, performed at the microarray Unit of CRG (Barcelona, Spain). Microarray analysis was performed with 3 animals each. Data was normalized using cyclic loess, and differentially expressed genes were identified using AFM 4.0 (ref. 48) for all pairwise comparisons. Raw data was taken from the Feature Extraction output files and was corrected for background noise using the normexp method. To assure comparability across samples quantile normalization was used. Differential expression analysis was carried out on non-control probes with an empirical Bayes approach on linear models (limma). Results were corrected for multiple testing according to the false discovery rate (FDR) method. Statistical analysis was performed with the Bioconductor project (http://www.bioconductor.org/) in the R statistical environment. Venn diagrams were generated using BioVenn[49].

***In vivo* treatments.** Autophagy of aged C57BL/6 and GFP–LC3 mice was induced as follows, one group of mice was injected i.p. with 4 mg per kg body weight of rapamycin (LC Laboratories) or vehicle (DMSO) every other day for 2 weeks; a second group was injected i.p. with 30 mg per kg body weight of Trolox (6-hydroxy-2,5,7,8-tetramethylchroman-2-carboxylic acid, Sigma) or vehicle (DMSO) daily for 2 weeks; and the third group of mice was treated with 3 mM spermidine (S2626 Sigma) in drinking water for 2 weeks.

Satellite cell engraftment. Satellite cell transplants were performed as in ref. 8, following an adapted protocol[50]. Quiescent FACS-isolated satellite cells were collected, re-suspended in 20% FBS Ham's F10 medium and injected into muscles of recipient mice previously injured with cardiotoxin the day before. The recipient mice were SCID mice. For each mouse, 10,000 cells were injected. At 4 days (for proliferation, senescence analyses) or 1 month (muscle regeneration) after cell injections, engrafted muscles were collected and processed for muscle histology. Results are expressed as relative number of GFP$^+$ per muscle section, with respect to the control data for young cells, which was set at 100% .

***In vitro* treatments.** Experiments for *in vitro* rescue of defective autophagy in satellite cells were performed in 20% FBS containing Ham's F10 medium (growth medium), and with the addition of either rapamycin (100 ng ml^{-1}, LC Laboratories), Trolox (100 μM , Sigma), spermidine (5 μM, Sigma) or vehicle (DMSO) for 48 h. Mitochondrial, lysosomal, and ROS analyses or ChIP experiments were performed immediately after treatments, whereas proliferation assays (BrdU staining) and senescence analysis (SA-β-gal assay and determination of RNA and protein expression of senescence markers), were performed 96 h after treatments.

For the satellite cell treatments for *in vivo* engraftment in injured muscles, fresh FACS-isolated satellite cells from resting muscle of young and geriatric mice were treated for 48 h with rapamycin (100 ng ml^{-1}, LC Laboratories), Trolox (100 μM, Sigma) or vehicle (DMSO) before engraftment into pre-injured muscles of recipient mice. For each mouse, 10,000 cells were injected. At 4 days after cell injections, engrafted muscles were collected and processed for muscle histology.

Bafilomycin (10 nM Sigma B1793) was used to block autophagy for 4 h at 37 °C and to analyse autophagosome accumulation by FACS, immunostaining and western blotting. CCCP (carbonyl cyanide 3-chlorophenylhydrazone, 10 μM Sigma C2759), which abolishes the link between the respiratory chain and the phosphorylation system in intact mitochondria, causes mitochondria uncoupling and was used to treat satellite cells *in vitro* for 1 h to induce the selective autophagy of CCCP-damaged mitochondria (mitophagy).

Plasmid transfection. Freshly isolated cells were transfected with mRFP–GFP–LC3 (ref. 23) plasmid using Lipofectamine 3000 (Invitrogene), and treated for 48 h with Trolox (25 μl ml^{-1}, Sigma) or vehicle (DMSO) and analysed on glass slides (Thermo Scientific 177402). Cells were fixed with 4% paraformaldehyde in PBS for 10 min and the nuclei were stained with DAPI (Invitrogen). After washing, glass slides were mounted with Mowiol. Measuring autophagy flux through this method is based on the concept of lysosomal quenching of GFP. GFP is a stably folded protein and relatively resistant to lysosomal proteases. However, the low pH inside the lysosome quenches the fluorescent signal of GFP, which makes it difficult to trace the delivery of GFP–LC3 to lysosomes. In contrast, RFP exhibits more stable fluorescence in acidic compartments, and mRFP–LC3 can be readily detected in autolysosomes. By exploiting the difference in the nature of these two fluorescent proteins (that is, lysosomal quenching of GFP fluorescence versus lysosomal stability of RFP fluorescence), autophagic flux can be morphologically traced with an mRFP–GFP–LC3 tandem construct[23]. With this tandem construct, autophagosomes and autolysosomes are labelled with yellow (mRFP and GFP) and red (mRFP only) signals, respectively.

Proliferation assay. Satellite cells were labelled with BrdU (1.5 μg ml^{-1}; Sigma) for 1 h. BrdU-labelled cells were detected by immunostaining using rat anti-BrdU antibody (Oxford Biotechnology; 1:500) and a specific secondary biotinylated goat anti-rat antibody (Jackson Inmunoresearch; 1:250). Antibody binding was visualized using Vectastain Elite ABC reagent (Vector Laboratories) and DAB. BrdU-positive cells were quantified as the percentage of the total number of cells analysed.

SA-β-gal activity. SA-β-gal activity was detected in satellite cells using the senescence β-galactosidase staining kit (Cell signaling), according to the manufacturer's instructions. SA-β-gal$^+$ cells were quantified as percentage of the total number of cells analysed.

Lentivirus infection. Freshly isolated satellite cells were *ex vivo* infected with distinct lentivirus for 12 h. Medium was replaced and cells were transplanted into injured muscle of recipient mice for *in vivo* analysis, or subjected to *in vitro* assays. LV-Atg7, used for Atg7 overexpression in satellite cells, was provided by Eliezer Masliah's laboratory[51]. LV-sh-p16^{INK4a}, used to silence *INK4a*, and LV-sh-scramble (used as control), were previously described in ref. 8.

Heterografting experiments. Extensor digitorum longus (EDL) muscles from geriatric wild-type mice were infected with lentivirus (LV-Atg7 or LV-GFP, as well as LV-sh-p16^{INK4a} or LV-sh-scramble) and grafted immediately onto the tibialis anterior muscle of young wild-type recipient mice, and regeneration

(formation of new myofibres derived from EDL-associated satellite cells) in the transplanted EDL muscles was analysed after 6 or 8 days. Fibre size of eMHC$^+$ myofibre was analysed using the Fiji program.

RT–qPCR: RNA extraction, cDNA synthesis and PCR. Total RNA was isolated from either FACS-isolated satellite cells of mouse muscle tissue or human myoblasts obtained from human muscle biopsies, using Tripure reagent (Roche Diagnostic Corporation) or RNeasy Micro kit (Qiagen), and analysed by RT–qPCR. For qPCR experiments, DNase digestion of 10 mg of RNA was performed using 2 U DNase (Turbo DNA-free, Ambion). Complementary DNA (cDNA) was synthesized from total RNA using the First-Strand cDNA Synthesis kit (Amersham Biosciences). Real-time PCR reactions were performed on a LightCycler 480 System using Light Cycler 480 SYBR Green I Master reaction mix (Roche Diagnostic Corporation) and specific primers. Thermocycling conditions were as follows: initial step of 10 min at 95 °C, then 50 cycles of 15 s denaturation at 94 °C, 10 s annealing at 60 °C and 15 s extension at 72 °C. Reactions were run in triplicate, and automatically detected threshold cycle values were compared between samples. Transcript of the ribosomal protein L7 housekeeping gene was used as endogenous control, with each unknown sample normalized to L7 content. The following primers were used, *INK4a*, forward: CATCTGGAGCAGCATGGAGTC, reverse: GGGTACGACCGAAAGAGTTCG; *p21^{CIP1}*, (also known as *Cdkn1a*) forward: CCAGGCCAA GATGGTGTCTT, reverse: TGAGAAAGGATCA GCCATTGC; *MyoD* (also known as *Myod1*), forward: GCCGCCTGAGC AAAGTGAATG, reverse: CAGCGGTCCAGGTGCGTAGAAG; *Mgn* (*Myog*), forward, GGTGTGTAAGAGGAAGTCTGTG, reverse: TAGGCGCTCAAT GTACTGGAT; *Ki67* (*Mki67*), forward, ACCGTGGAGTAGTTTATCTGGG, reverse, TGTTTCCAGTCCGCTT-ACTTCT; *p15^{INK4b}* (also known as *Cdkn2b*), forward, TCTTGCATCTCCACCAGCTG, reverse, CTCCAGGTTTCCCA TTTAGC; *Atg7*, forward, TCTGGGAAGCCATAAAGTCAGG, reverse, GCGAAGGTCAGGAGCAGAA.

Electron microscopy images. For electron microscopy images, tibialis anterior muscles from 3- and 24-month-old wild-type mice were fixed with 2% paraformaldehyde and 2.5% glutaraldehyde in phosphate buffer (0.1 M, pH 7.4). Samples were processed by the CCit Microscopy Facility at the University of Barcelona. Images were acquired using a Jeol 1010 microscope, working at 80 kV and equipped with a CCD Megaview III camera. Identification of satellite cells in skeletal muscle by electron microscopy was based on cell size, content of heterochromatin and position with respect to basal lamina.

Western blotting. Preparation of mouse and human satellite cell lysates and western blotting was performed as described previously in ref. 52. Antibodies used were: anti-p62/SQSTM1 antibody produced in rabbit (Sigma P0067), rabbit anti-LC3 (Novus Biologicals NB100-2331), phospho-S6 ribosomal protein (Ser240/244) XP rabbit monoclonal antibody (Cell Signaling 5364), rabbit anti-p16 (Santa Cruz Biotechnology sc-1207), rabbit anti-parkin (Abcam ab15954), S6 ribosomal protein (54D2) mouse (Cell Signaling 2317), γH2AX Ser 139 (Cell Signaling 2577S), rabbit anti-53BP1 (Abcam ab21083) and Tubulin (Sigma T-6199).

ChIP. Briefly, freshly isolated satellite cells were cultured with Trolox or vehicle (DMSO) for 48 h and crosslinked with 1% formaldehyde for 15 min at room temperature. For each ChIP, 300,000 cells were lysed in 130 μl of lysis buffer B (Low Cell ChIP Kit, Diagenode) and chromatin was sonicated for 10 min in a M220 Focused-ultrasonicator, Covaris (Duty cycle 5%, Peak incident power 75 W and 200 cycles per burst). Sonicated chromatin was then diluted and subjected to immunoprecipitation with 3 μl of antibody against ubquitinated histone (Ubiquityl-Histone) H2A (Lys119) (D27C4) (Cell Signaling, 8240) or 3 μl of IgG. Bound fraction and input were analysed by qPCR using specific primer sets for the *INK4a* locus. INK4a_RD forward, GGTCTCCCCTAGCAGGATTC, reverse GCCTGTCATTAAACAGGGTGA; INK4a_exon1 forward, CCGGAGCCACCCATTAAACTA, reverse CAAGACTT CTCAAAAATAAGACACTGAAA; INK4a_exon2 forward, CCCAACACCC ACTTGAGGAA, reverse, CAGAGGTCACAGGCATCGAA.

Histology and immunohistochemistry in muscle cryosections. Tibialis anterior and extensor digitorum longus (EDL) muscles were frozen in isopentane cooled with liquid nitrogen, and stored at −80 °C until analysis. Then 10-μm sections were collected from muscles and were either stained with haematoxylin and eosin or immunostained. Labelling of cryosections with mouse monoclonal primary antibodies was performed using the peroxidase or fluorescein M.O.M. kit staining (Vector Laboratories) according to the manufacturer's instructions. Double immunostaining was performed by sequential addition of each primary and secondary antibody using appropriate positive and negative controls. Sections were air dried, fixed on 2–4% paraformaldehyde, washed on PBS and incubated with primary antibodies according to manufacturer's instructions after blocking for 1 h at room temperature with a high-protein-containing solution in PBS (Vector Laboratories). The slides were then washed with PBS and incubated with the appropriate secondary antibodies and labelling dyes. For immunofluorescence, secondary antibodies were coupled to Alexa-488, Alexa-568 or Alexa-647 fluorochromes, and nuclei were stained with DAPI (Invitrogen). After washing, tissue sections were mounted with Mowiol.

Antibodies used for immunohistochemistry. Immunohistochemistry on muscle cryosections or isolated satellite cells was performed with the following antibodies: GFP (Invitrogen A6455 and Aves labs GFP-1020), anti-eMHC (F1.652), anti-Pax7 (DSHB), p16 (Santa Cruz sc-1207), γH2AX Ser139 (2577S), rabbit polyclonal anti-MyoD (Santa Cruz Biotechnology sc-760), anti-myogenin (DSHB F5D), poly-ubiquitinylated proteins, multi-ubiquitin chains, mouse monoclonal antibody (Enzo life sciences PW8805), anti-p62/SQSTM1 antibody produced in rabbit (Sigma P0067), mouse monoclonal antibody to LC3 (NanoTools 5F10), LAMP-1 (Santa Cruz Biotechnology sc-19992), phospho-S6 ribosomal protein (Ser240/244) XP rabbit monoclonal antibody (Cell Signaling 5364), anti-CD56 (BD Pharmingen 556325), anti-TOM20 (ab56783).

Human muscle samples. Muscle biopsies from 8 adults and 10 geriatric (28 ± 7 and 83 ± 7 years old, respectively) human subjects were obtained via the Tissue Banks for Research from Vall d'Hebron and Sant Joan de Deu Hospitals and especially via the EU/FP7 Myoage Consortium. Muscle biopsies were taken from the vastus lateralis muscle under local anaesthesia (2% lidocaine). A portion of the muscle tissue was directly frozen in melting isopentane and stored at −80 °C until analysis. Human primary myoblasts from 5 young/adult (25 ± 4 years old) and 5 geriatric (75 ± 4 years old) subjects were obtained from the EU/FP7 Myoage Consortium or purchased from Cook Myosite and cultured following the provided instructions.

Digital image acquisition and processing. Digital images were acquired using: (1) an upright microscope DMR6000B (Leica) equipped with a DFC300FX camera for immunohistochemical colour pictures and a Hamamatsu ORCA-ER camera for immunofluorescence pictures; (2) confocal images of muscle sections or isolated satellite cells were taken using either a Zeiss LSM-780 confocal system with a Plan-Apochromat 63 × /1.4 NA oil objective or a Leica SPE confocal laser scanning microscope system with HCX PL Fluotar 10 × /0.30 NA, 20 × /0.50 NA and 40 × /0.75 NA objectives. The different fluorophores (3 to 4) were excited using the 405, 488, 568 and 633 nmexcitation lines. Acquisition was performed using Zeiss LSM software Zen Black or Leica Application or LAS AF software (Leica). Images were composed and edited in Photoshop CS5 (Adobe), in which background was reduced using brightness and contrast adjustments applied to the whole image. To assess myofibre size, individual fibres were manually outlined and their cross-sectional area (CSA) was determined with the public domain image analysis software Fiji. Fluorescence intensity of selected proteins for each cell was quantified using Fiji software and the average of relative fluorescence was expressed as MFI.

The number and percentage of cellular area occupied by GFP–LC3 puncta were determined on digital images with Fiji and the cell image analysis software CellProfiler[53]. Co-localization of RFP–LC3 and GFP–LC3 puncta was determined on the maximum projection of three *z*-sections using a Fiji automated macro pipeline calculating single and double-positive autophagosomes. Co-localization of p62 and ubiquitin was determined on digital images Fiji, according to ref. 54, with respect to the total cellular area. The Pearson's coefficient (*r*) was used to analyse the correlation of the intensity values of green and red pixels in dual-channel images. This coefficient measures the strength of the linear relationship between the intensities in two images calculated by linear regression and ranges from 1 to ×1, with 1 standing for complete positive correlation and ×1 for a negative correlation, with zero standing for no correlation[51]. Video reconstructions of autophagosomes were generated in Imaris software using full confocal *z*-stacks (around 20) of each cell. The *z*-stacks were previously imported to Fiji software for background adjustments and then deconvolved using the blind-deconvolution wizard in Huygens software.

Statistical analysis. For mouse experiments, no specific blinding method was used, but mice in each sample group were selected randomly. The sample size (*n*) of each experimental group is described in each corresponding figure legend, and all experiments were repeated at least with three biological replicates. GraphPad Prism software was used for all statistical analyses. Quantitative data displayed as histograms are expressed as means ± standard error of the mean (represented as error bars). Results from each group were averaged and used to calculate descriptive statistics. Mann–Whitney *U*-test (independent samples, two-sided) was used for pairwise comparisons among groups at each time point. Statistical significance was set at a $P < 0.05$.

46. Masiero, E. *et al.* Autophagy is required to maintain muscle mass. *Cell Metab.* **10,** 507–515 (2009).
47. Suelves, M. *et al.* uPA deficiency exacerbates muscular dystrophy in MDX mice. *J. Cell Biol.* **178,** 1039–1051 (2007).
48. Breitkreutz, B. J., Jorgensen, P., Breitkreutz, A. & Tyers, M. AFM 4.0: a toolbox for DNA microarray analysis. *Genome Biol.* **2,** http://dx.doi.org/10.1186/gb-2001-2-8-software0001 (2001).
49. Hulsen, T., de Vlieg, J. & Alkema, W. BioVenn—a web application for the comparison and visualization of biological lists using area-proportional Venn diagrams. *BMC Genomics* **9,** 488 (2008).
50. Sacco, A. *et al.* Short telomeres and stem cell exhaustion model Duchenne muscular dystrophy in mdx/mTR mice. *Cell* **143,** 1059–1071 (2010).
51. Crews, L. *et al.* Selective molecular alterations in the autophagy pathway in patients with Lewy body disease and in models of α-synucleinopathy. *PLoS ONE* **5,** e9313 (2010).
52. Perdiguero, E. *et al.* Genetic analysis of p38 MAP kinases in myogenesis: fundamental role of p38α in abrogating myoblast proliferation. *EMBO J.* **26,** 1245–1256 (2007).
53. Kamentsky, L. *et al.* Improved structure, function and compatibility for CellProfiler: modular high-throughput image analysis software. *Bioinformatics* **27,** 1179–1180 (2011).
54. Bolte, S. & Cordelieres, F. P. A guided tour into subcellular colocalization analysis in light microscopy. *J. Microsc.* **224,** 213–232 (2006).

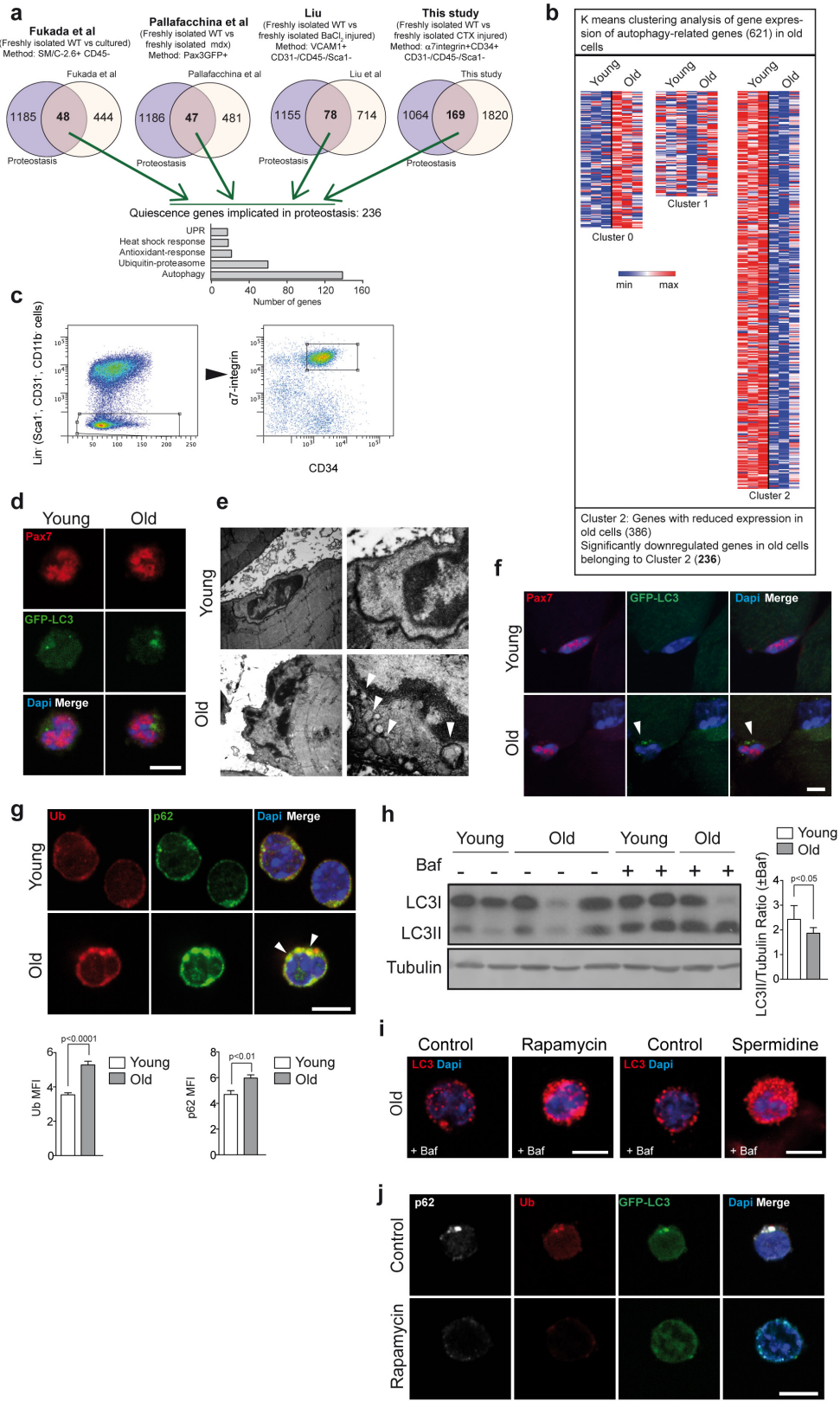

Extended Data Figure 1 | See next page for caption.

Extended Data Figure 1 | The reduced autophagy flux in quiescent satellite cells can be increased by pharmacological treatment *in vivo*. **a**, Venn diagrams of overlapping genes between a proteostasis gene set (See Supplementary Table 1) and genes significantly upregulated in quiescent satellite cells from the indicated publications or from our gene expression microarray data comparing freshly FACS isolated satellite cells from resting muscle, or muscles obtained 72 h after cardiotoxin (CTX) injury, from young, wild-type mice. **b**, *K*-means clustering analysis (performed with Gene-E, Broad Institute) of the gene expression of the autophagy-related genes during ageing. Clusters are shown with heat maps of the normalized raw data. Each column represents a different sample and each row a different gene probe. Red, increased expression; white, neutral expression; blue, decreased expression. **c**, Representative example of the FACS strategy and gating scheme for isolating satellite cells from mice in resting conditions. **d**, Pax7 and GFP immunostaining of freshly isolated satellite cells from resting muscles of young and old GFP–LC3 mice. Scale bar, 5 μm. **e**, Electron microscopy images of young and old satellite cells on sections of resting tibialis anterior (TA) muscle of wild-type (WT) mice. Arrowheads indicate autophagic vesicles. Scale bars, 1 μm and 0.5 μm (right and left, respectively). **f**, Pax7 and GFP immunostaining on tissue sections from resting tibialis anterior muscles of young and old GFP–LC3 mice. Arrowheads indicate autophagic vesicles. Scale bar, 5 μm. **g**, p62 and ubiquitin (Ub) MFI. Arrowheads, co-localization of p62 and ubiquitin aggregates. **h**, LC3 western blot of freshly isolated satellite cells from young and old, wild-type mice, treated with bafilomycin or vehicle for 4 h before collection. Graph shows LC3II quantification, after normalization with tubulin levels; for full scan see Supplementary Fig. 2. **i**, Quiescent satellite cells were freshly isolated from old, wild-type mice subjected to two weeks of rapamycin, spermidine or vehicle (control) treatment. Cells were treated (or not treated) with bafilomycin 4 h prior to analysis by immunostaining of LC3 marker. *Z* projections of representative fluorescence microscopy images are shown. Scale bars, 5 μm. **j**, Representative fluorescent microscopy images from Fig. 1d. Scale bar, 5 μm. Data show mean ± s.e.m. Comparisons by two-sided Mann–Whitney *U*-test. *P* values are indicated. Number of samples were $n = 3$ animals per group for **a** and **b**; $n = 35$ (young) and 66 (old) cells analysed from 3 animals for **g**; $n = 3$ animals per group for **h**.

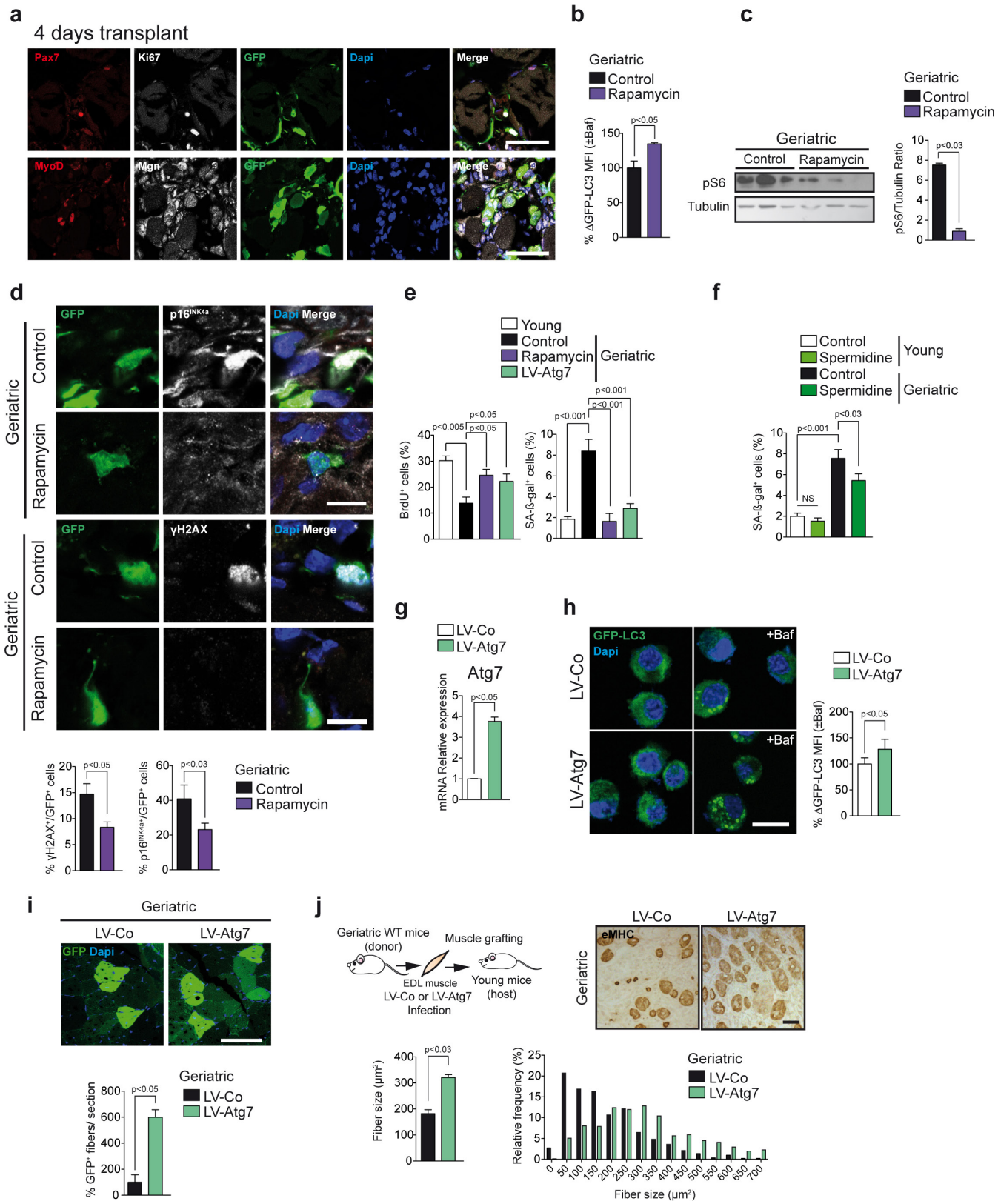

Extended Data Figure 2 | See next page for caption.

Extended Data Figure 2 | Reinduction of autophagy rescues proliferation and reduces senescence in geriatric satellite, thus restoring regenerative capacity. **a**, Transplanted muscles from Fig. 2c were immunostained for GFP and for Ki67, Pax7, MyoD or Mgn (to determine the distinct possible myogenic states of satellite cells in the regenerating muscle). Scale bars, 50 μm. **b**, Autophagy flux analysed by flow cytometry in freshly isolated satellite cells from resting muscle of GFP–LC3 mice, treated for 48 h with rapamycin or vehicle (control). Satellite cells were treated with bafilomycin or vehicle for 4 h before analysis. Results are expressed as the change in GFP–LC3 MFI in bafilomycin (−) compared to bafilomycin (+) conditions. **c**, Western blot analysis of pS6 protein levels in geriatric satellite cells from wild-type mice, treated for 48 h with rapamycin or vehicle (control). Graph shows pS6 quantification, normalized to tubulin; for full scan see Supplementary Information Fig. 2. **d**, As in Fig. 2c, percentage $\gamma H2AX^+$ or $p16^{INK4a+}$cells from total GFP^+ cells were quantified. Scale bars, 10 μm. **e**, Quantification $BrdU^+$ and senescence-associated β-gal^+ satellite cells, pre-treated as in Fig. 2c and analysed after 96 h. **f**, Quantification of senescent (senescence-associated β-gal^+) satellite cells, isolated from young and geriatric wild-type mice, pre-treated for 48 h with spermidine or vehicle (control) and cultured for 96 h. **g**, Quantitative real-time PCR (RT–qPCR) analysis of Atg7 expression on satellite cells infected with LV-Atg7 or LV-control (LV-Co), and cultured for 96 h. **h**, GFP–LC3 satellite cells were infected with LV-Atg7 or LV-Co and treated with bafilomycin or vehicle for 4 h before analysis. Autophagy flux was analysed by flow cytometry and represented as in **b**. Representative images are shown. Scale bar, 10 μm. **i**, Muscle regeneration experiment by satellite cell transplantation. An equal number of satellite cells from young and geriatric mice infected with a lentivirus overexpressing the *Atg7* gene (LV-Atg7) or a lentivirus control (LV-Co), which also expressed GFP, were transplanted into injured muscle of young immunodeficient mice, and collected 28 days later. GFP expression in muscles was analysed by immunostaining. Quantification of GFP^+ cells (fibres) per muscle field versus transplanted control-treated satellite cells. Representative images are shown. Scale bar, 75 μm. **j**, EDL geriatric muscles, infected with LV-Atg7 or LV-Co, and grafted on recipient mouse muscle. Regeneration was analysed 8 days later. Frequency distribution of regenerating fibres by size. Scale bar, 25 μm. Data are mean ± s.e.m. Comparisons by two-sided Mann–Whitney *U*-test. *P* values are indicated. Number of samples were $n = 60{,}000$ cells analysed from 3 animals for **b**; $n = 3$ animals per group for **c**; $n = 5$ engraftments per group for **d**; $n = 3$ animals per group for **e**–**g**; $n = 60{,}000$ cells analysed from 3 animals for **h**; $n = 3$ engraftments per group for **i**; $n = 4$ engraftments per group for **j**.

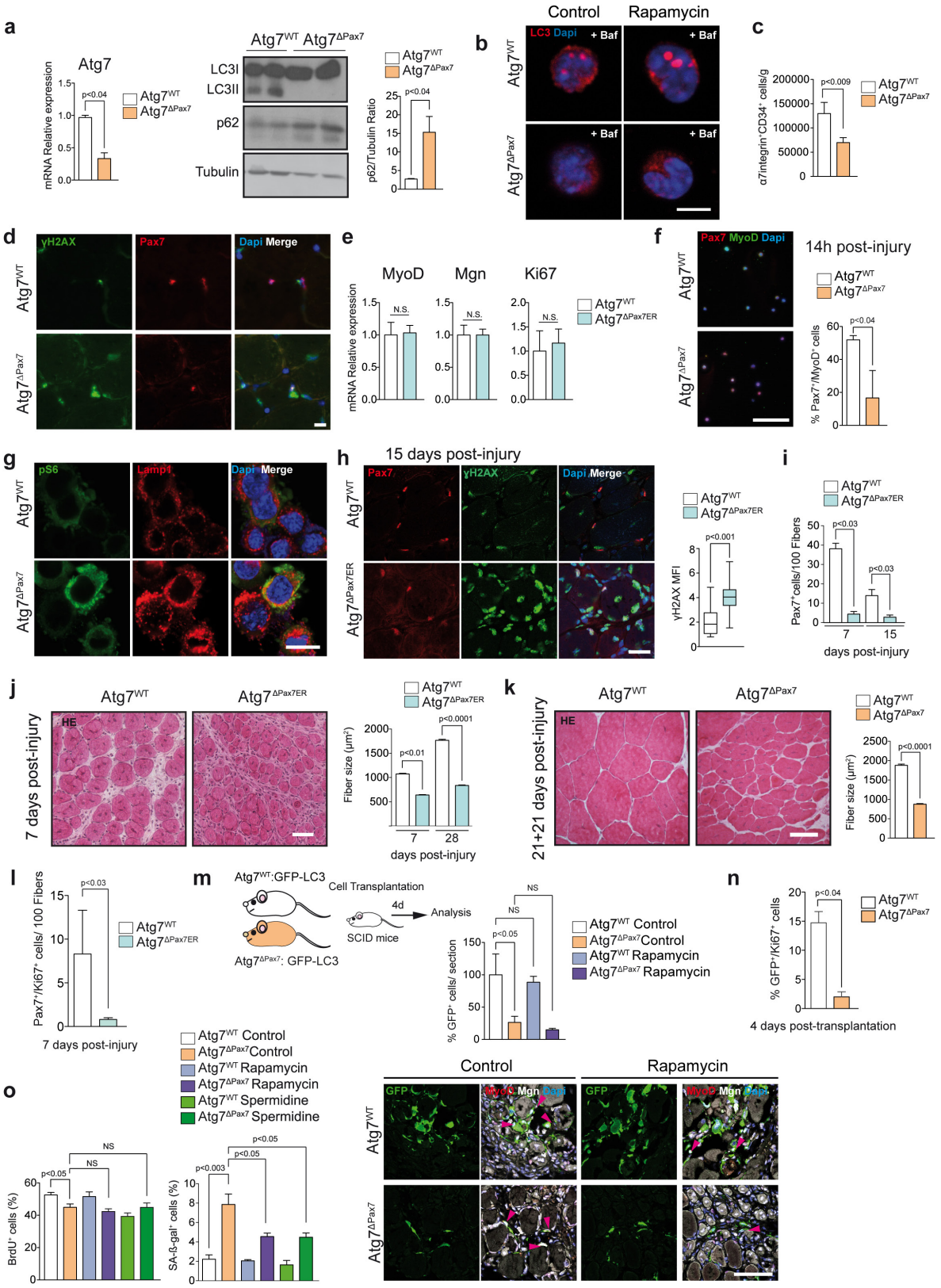

Extended Data Figure 3 | See next page for caption.

Extended Data Figure 3 | Genetic impairment of autophagy in young quiescent satellite cells leads to premature senescence and impaired muscle regeneration. **a**, RT–qPCR analysis of *Atg7* expression and western blot analysis of LC3, p62 and tubulin of satellite cells isolated from $Atg7^{WT}$ and $Atg7^{\Delta Pax7}$ mice. Graph shows the quantification of p62 normalized to tubulin; for full scan see Supplementary Fig. 2. **b**, Quiescent satellite cells were freshly isolated from $Atg7^{WT}$ and $Atg7^{\Delta Pax7}$ mice which had been subjected to two weeks of rapamycin or vehicle (control) treatment *in vivo*. Cells were treated (or controls were untreated) with bafilomycin 4 h before analysis by fluorescence microscopy. *Z* projections of representative fluorescence microscopy images are shown. Scale bar, 5 μm. **c**, Quantification of satellite cells in resting muscle of three-month-old $Atg7^{WT}$ and $Atg7^{\Delta Pax7}$ mice by flow cytometry analysis ($\alpha7$ integrin$^+$CD34$^+$ cells per gram of muscle tissue). **d**, Representative fluorescent microscopy images from Fig. 3d. Scale bar, 10 μm. **e**, RT–qPCR analysis of MyoD, Mgn and Ki67 expression in freshly isolated quiescent satellite cells from resting muscle of $Atg7^{WT}$ and $Atg7^{\Delta Pax7ER}$ mice, 7 days after tamoxifen treatment. **f**, Percentage of activated satellite cells (Pax7$^+$/MyoD$^+$) from the total Pax7$^+$ cells (FACS-isolated 14-h post-injury from (**a**)). Scale bar, 50 μm. **g**, pS6 and Lamp1 immunostaining of cells from **a**. Scale bar, 10 μm. **h**, γH2AX protein levels per nucleus in Pax7$^+$ satellite cells in tibialis anterior muscles of $Atg7^{WT}$ and $Atg7^{\Delta Pax7ER}$ mice, 15 days post-injury. Representative images are shown. Scale bar, 25 μm. **i**, Pax7$^+$ satellite cells were quantified following immunostaining on regenerating muscles of $Atg7^{WT}$ and $Atg7^{\Delta Pax7ER}$ mice 7 days and 15 days after cardiotoxin injury. **j**, Representative images of haematoxylin and eosin staining of muscles at 7 days post-injury on muscles of $Atg7^{WT}$ and $Atg7^{\Delta Pax7ER}$ mice. Fibre size of central-nucleated myofibres at 7 days and 28 days post-injury is quantified. Scale bar, 50 μm. **k**, Tibialis anterior muscles of $Atg7^{WT}$ and $Atg7^{\Delta Pax7}$ mice were injured by cardiotoxin injection and 21 days later these muscles were reinjured and then subsequently analysed 21 days later (21 + 21 days post-injury). The size of central-nucleated myofibres was quantified. Representative images are shown. Scale bar, 50 μm. **l**, Pax7$^+$ and Ki67$^+$ double-positive satellite cells were quantified following immunostaining on regenerating muscles of $Atg7^{WT}$ and $Atg7^{\Delta Pax7ER}$ mice 7 days after cardiotoxin injury. **m**, An equal number of quiescent satellite cells from $Atg7^{WT}$:GFP–LC3 and $Atg7^{\Delta Pax7}$:GFP–LC3 mice (two weeks ± rapamycin pre-treatment), transplanted as in Fig. 2c, and immunostained with the indicated antibodies 4 days later. Quantification of GFP$^+$ cells per muscle field. Values relative to transplanted young cells (100%). Representative images are shown. Scale bar, 75 μm. **n**, Percentage of GFP$^+$ cells that are also Ki67$^+$ cells in muscles from **m**. **o**, Quantification of proliferating (BrdU$^+$) and senescent (SA-β-gal$^+$) satellite cells, isolated from $Atg7^{WT}$ and $Atg7^{\Delta Pax7}$, pre-treated for 48 h with spermidine or rapamycin (or control vehicle) and cultured for 96 h. Data show mean ± s.e.m. Comparisons by two-sided Mann–Whitney *U*-test. *P* values are indicated. The number of samples were $n = 3$ animals per group (**a**); $n = 7$ animals per group (**c**); $n = 3$ animals per group (**e**–**l**); $n = 4$ engraftments per group (**m**, **n**); $n = 3$ animals per group (**o**).

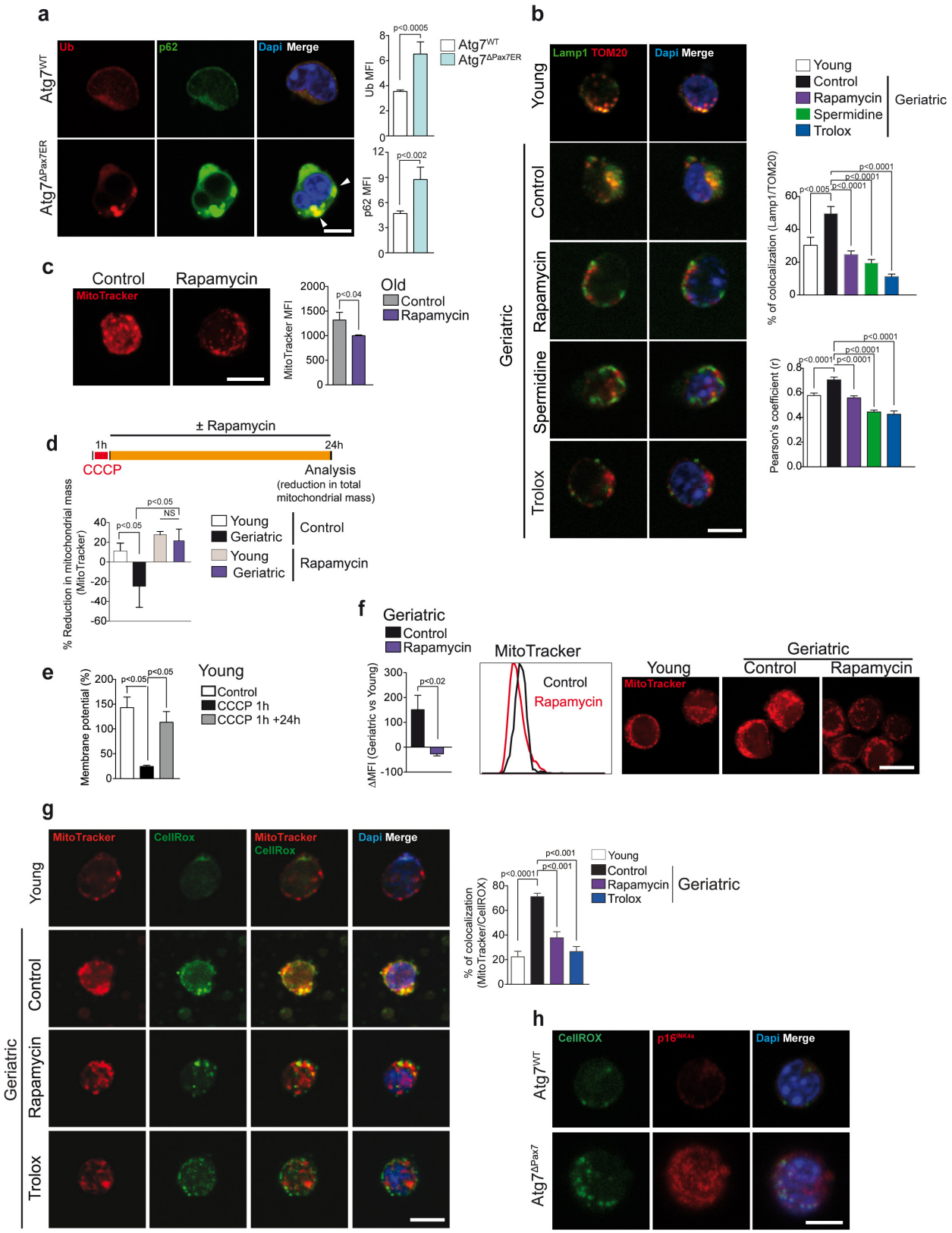

Extended Data Figure 4 | See next page for caption.

Extended Data Figure 4 | Autophagy loss in satellite cells causes dysfunctional mitophagy and mitochondria accumulation, leading to increased ROS and senescence. a, p62 and ubiquitin immunostaining on freshly isolated satellite cells from resting muscle of three-month-old $Atg7^{WT}$ and $Atg7^{\Delta Pax7ER}$ mice, one month after tamoxifen treatment. Arrowheads indicate co-localization of p62 and Ub aggregates. Representative images are shown. Scale bar, 5 μm. **b**, TOM20 and Lamp1 immunostaining of quiescent satellite cells isolated from young and geriatric WT mice. Mice were subjected to two weeks of rapamycin, spermidine or Trolox (or vehicle) treatment before analysis. Co-localization was calculated as the area occupied by the immunofluorescence co-localizing staining on images with respect to the total cellular area. The Pearson's coefficient (r) was used to analyse the correlation of the intensity values of green and red pixels in the dual-channel images. The z projections of representative fluorescence microscopy images are shown. Scale bar, 5 μm. **c**, Mitochondria quantification by MitoTracker in quiescent satellite cells of old mice, treated with rapamycin or vehicle for two weeks. **d**, Mitochondria (MitoTracker labelling) in young or geriatric cells. Satellite cells, were pre-treated with CCCP for 1 h (see Methods) and ± rapamycin for 24 h. Percentage of MitoTracker MFI reduction ± rapamycin. **e**, For the mitochondrial membrane potential analysis, satellite cells were freshly isolated from young wild-type mice and treated for 1 h with CCCP or DMSO (control). Membrane potential (TMRM MFI/MitoTracker Green MFI ratio) of cells was calculated by flow cytometry analysis at 1 h and 24 h after CCCP treatment (being 100% the membrane potential value of control satellite cells). **f**, Mitochondria content was quantified by MitoTracker staining of satellite cells from young and geriatric wild-type mice treated with rapamycin or vehicle (control) for 48 h. The z projections of representative fluorescence microscopy images are shown. Scale bar, 5 μm. **g**, Mitochondria and ROS detection by MitoTracker and CellROX staining, respectively. Co-localization was calculated as in **b**. The z projections of representative fluorescence microscopy images are shown. Scale bar, 5 μm. **h**, Representative images of freshly isolated satellite cells from resting muscle of three-month-old $Atg7^{WT}$ and $Atg7^{\Delta Pax7}$ mice stained with CellROX fluorescent dye and $p16^{INK4a}$ antibody. Scale bar, 5 μm. Data are mean ± s.e.m. Comparisons by two-sided Mann–Whitney U-test. P values are indicated. Number of samples were $n = 36$ ($Atg7^{WT}$) and $n = 38$ ($Atg7^{\Delta Pax7ER}$) cells analysed from 3 animals (**a**); $n = 23$ (young), $n = 24$ (control), $n = 42$ (rapamycin); $n = 28$ (spermidine) and $n = 21$ (Trolox) cells analysed from 3 animals (**b**); $n = 60{,}000$ cells analysed from 3 animals (**c**); $n = 40{,}000$ cells analysed from 4 animals (**d**); $n = 30{,}000$ cells analysed from 3 animals (**e**, **f**); $n = 18$ (young), 21 (control), 15 (rapamycin) and 13 (Trolox) cells analysed from 3 animals (**g**).

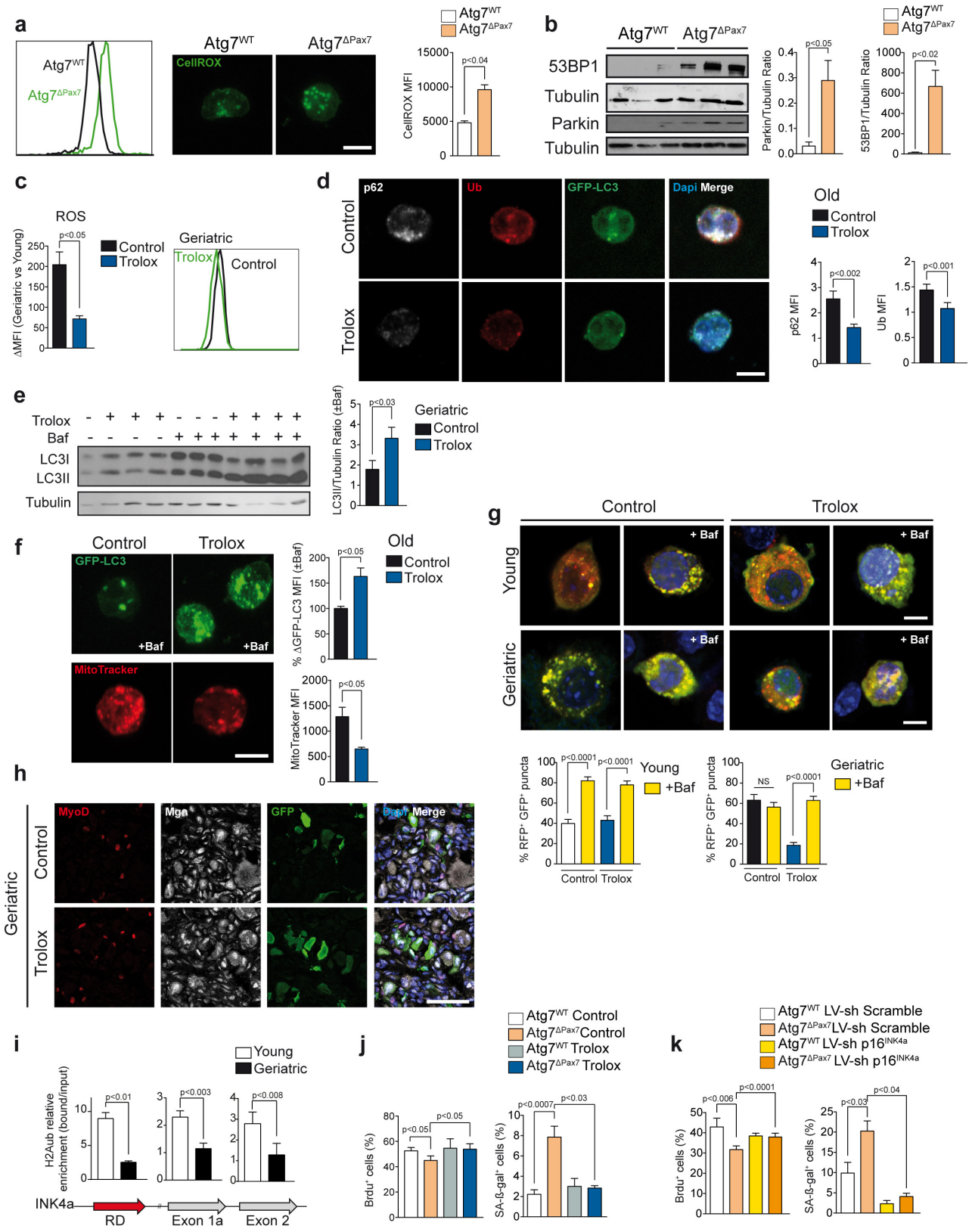

Extended Data Figure 5 | See next page for caption.

Extended Data Figure 5 | ROS inhibition in autophagy-impaired aged and *Atg7* null satellite cells significantly restores cell proteostasis. **a**, ROS-level quantification in quiescent satellite cells from three-month-old $Atg7^{WT}$ and $Atg7^{\Delta Pax7}$ mice by CellROX flow cytometry. Representative images are shown. Scale bar, 5 μm. **b**, Western blot analysis of 53BP1 and parkin in satellite cells isolated from three-month-old $Atg7^{WT}$ and $Atg7^{\Delta Pax7}$ mice. Tubulin control is the same tubulin control for Fig. 3g. Graph shows quantification of 53BP1 and parkin protein normalized to tubulin; for full scan see Supplementary Information Fig. 1. **c**, Quantification of ROS levels for satellite cells isolated from young and geriatric WT mice by flow cytometry using CellROX fluorescent dye. Satellite cells were treated with Trolox or vehicle (control) for 48 h before analysis. Results are represented as variation of MFI between young and geriatric satellite cells. **d**, Quantification of p62 and ubiquitin protein levels on immunostained freshly isolated satellite cells from resting muscle of old wild-type mice, *in vivo* treated for 2 weeks with Trolox or vehicle (control). Representative images are shown. Scale bar, 5 μm. **e**, Western blot analysis of LC3 and tubulin in satellite cells isolated from geriatric WT mice and treated for 48 h with Trolox or vehicle (control), in the absence or presence of bafilomycin for 4 h before analysis. Graph shows quantification of LC3II protein normalized to tubulin; for full gel scan see Supplementary Information Fig. 2. **f**, Autophagy flux and mitochondria in satellite cells from GFP–LC3 mice (two weeks with or without Trolox treatment). Satellite cells treated for 4 h ± bafilomycin treatment. Representative images are shown. Scale bar, 5 μm. **g**, The mRFP–GFP–LC3 plasmid was transfected into young or geriatric satellite cells, with 48 h treatment ± Trolox and then 4 h treatment ± bafilomycin, prior to fixation. The percentage of autophagosomes was quantified as in Fig. 2a. **h**, Muscle regeneration using geriatric satellite cell transplantation. An equal number of freshly isolated geriatric satellite cells, infected with GFP lentivirus and treated for 48 h with Trolox or vehicle, were transplanted into injured muscle of young immunodeficient mice. Four days later, muscles were collected and immunostained for GFP, MyoD and Mgn (to determine the possible myogenic states of satellite cells in the regenerating muscle). Representative images are shown. Scale bar, 50 μm. **i**, ChIP analysis for H2AK119ub (H2Aub) in satellite cells isolated from young and geriatric wild-type mice. **j**, Quantification of proliferating ($BrdU^+$) and senescent (SA-β-gal^+) satellite cells isolated from $Atg7^{WT}$ and $Atg7^{\Delta Pax7}$ mice treated 48 h with Trolox or vehicle (control) and cultured for 96 h. **k**, Quantification of proliferating ($BrdU^+$) and senescent (senescence-associated β-gal^+) satellite cells isolated from $Atg7^{WT}$ and $Atg7^{\Delta Pax7}$ mice and infected with LV-sh $p16^{INK4a}$ or LV-sh scramble, and cultured for 96 h. Data show mean ± s.e.m. Comparisons by two-sided Mann–Whitney *U*-tests. *P* values are indicated. Number of samples were $n = 60{,}000$ cells analysed from 3 animals (**a**); $n = 3$ animals per group (**b**); $n = 60{,}000$ cells analysed from 3 animals (**c**); $n = 36$ (control) and $n = 35$ (Trolox) cells analysed from 3 animals (**d**); $n = 3$ animals per group (**e**); $n = 60{,}000$ cells analysed from 3 animals (**f**); $n = 21$ (young), $n = 20$ (young, Trolox), $n = 19$ (young, + bafilomycin), $n = 18$ (young, Trolox + bafilomycin), $n = 21$ (geriatric), $n = 19$ (geriatric, Trolox), $n = 15$ (geriatric, + bafilomycin) and $n = 37$ (geriatric, Trolox + bafilomycin) cells analysed from 3 animals (**g**); $n = 3$ animals per group (**i**–**k**).

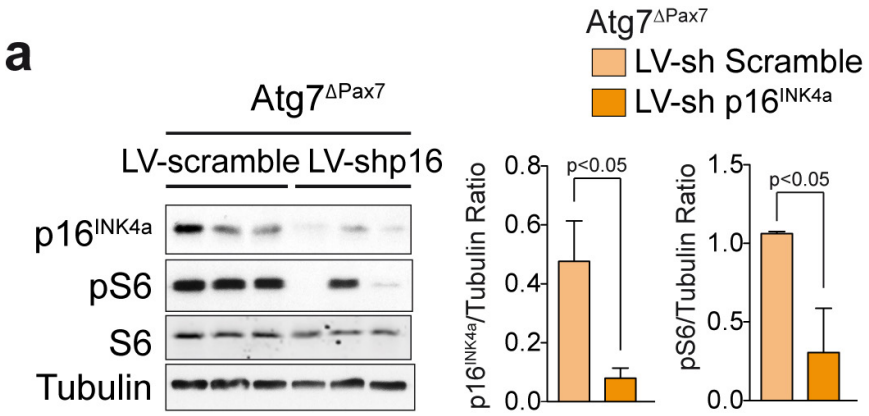

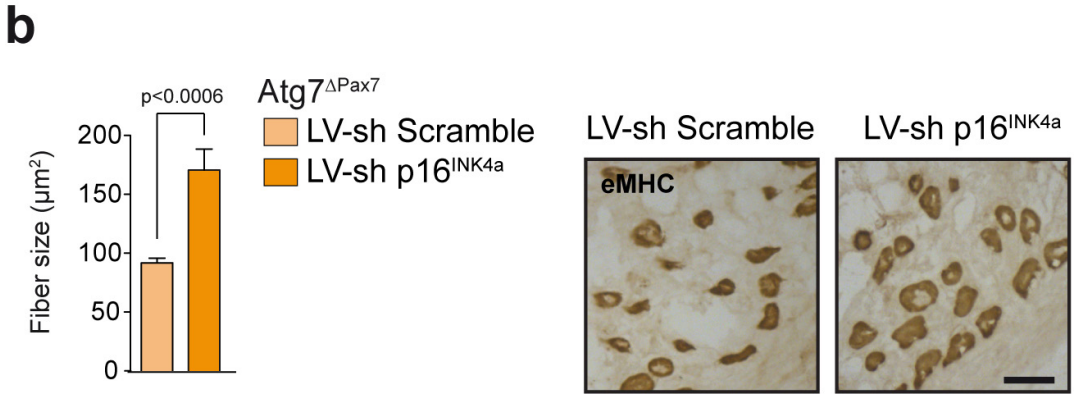

Extended Data Figure 6 | Effects of p16^{INK4a} silencing in autophagy-impaired young murine satellite cells. a, Western blotting quantification of Atg7$^{\Delta Pax7}$ satellite cells, infected with lentiviral LV-sh-p16^{INK4a} or LV-sh-scramble and analysed 96 h later; for full gel scan see Supplementary Fig. 2. **b**, Atg7^{WT} and Atg7$^{\Delta Pax7}$ EDL, infected with LV-sh-p16^{INK4a} or LV-sh-scramble, and grafted as Extended Data Fig. 2j. Representative eMHC-immunostaining. Scale bar, 25 μm. Data show mean ± s.e.m. Comparisons by two-sided Mann–Whitney *U*-test. *P* values are indicated. The number of samples were $n = 3$ animals per group (**a**) and $n = 4$ engraftments per group (**b**).

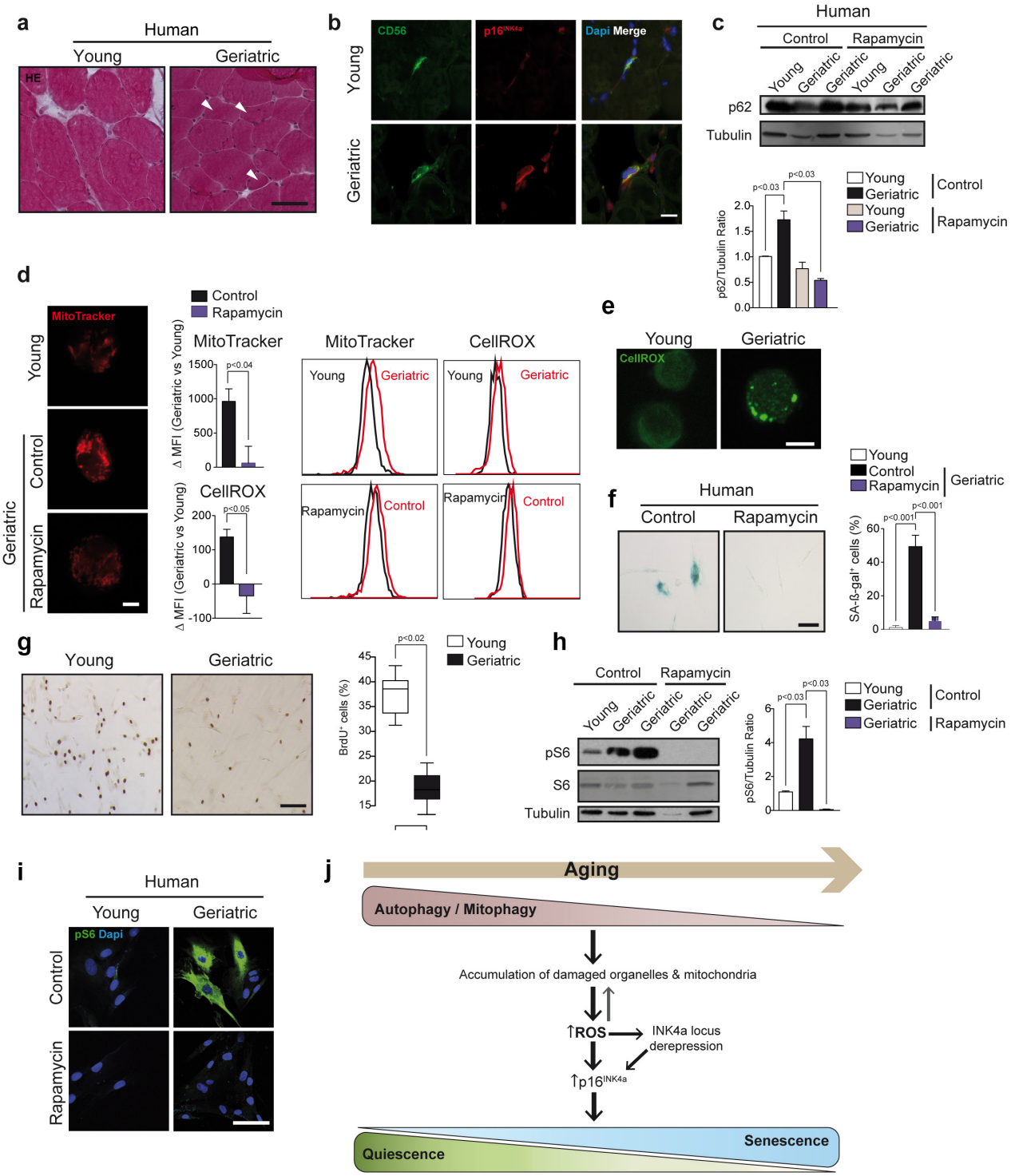

Extended Data Figure 7 | Impaired autophagic flux in human geriatric satellite cells. a, Representative images of haematoxylin and eosin staining of human muscle biopsies from young (25 years old) and geriatric (95 years old) donors in resting conditions. Arrowheads indicate atrophic myofibres. Scale bar, 50 μm. **b**, CD56 and p16^{INK4a} immunostaining on human muscle sections of samples described in **a**. Scale bar, 10 μm. **c**, Western blotting analysis of p62 protein in human satellite cells from young (about 25 years old) and geriatric (over 75 years old) donors, treated for 48 h ± rapamycin; for full gel scan see Supplementary Fig. 2. **d**, ROS and mitochondrial content analysis in human cells from treated for 48 h ± rapamycin. Graphs show MFI variation. Scale bar, 5 μm. **e**, Representative images from CellROX staining from **d**. Scale bar, 5 μm. **f**, Quantification of SA-β-gal^{+} human cells treated for 48 h ± rapamycin. Quantification was carried out 96 h after treatment. Scale bar, 200 μm. **g**, Quantification of proliferating (BrdU^{+}) young and geriatric human satellite cells in culture. Representative pictures are shown. Scale bar, 25 μm. **h**, Western blot analysis of pS6, total S6 and tubulin in young and geriatric human satellite cells treated for 48 h with rapamycin or vehicle (control). Graphs show p62 quantification normalized to tubulin; for full scan see Supplementary Information Fig. 2. **i**, Immunostaining of pS6 in young and geriatric human satellite cells treated as in **h**. Scale bar, 75 μm. **j**, Scheme showing the proposed model of how age-impaired autophagy leads to muscle stem-cell senescence and regenerative decline. Data show mean ± s.e.m. Comparisons by two-sided Mann–Whitney *U*-tests. *P* values are indicated. The number of samples were $n = 3$ human donors per group (**a**–**c**); $n = 60{,}000$ cells analysed from 3 human donors (**d**), $n = 3$ human donors per group (**f**–**h**).